Spectro - Photometric study of star forming early type galaxies

S. P. Deshmukh[1,*]

[1]Department of Physics, Institute of Science, Nagpur 440001, India

[*]Corresponding Author: deshmukhsp18@gmail.com

Abstract We combine the results of optical spectroscopy and photometry of a sample of local early type galaxies by Sloan Digital Sky Survey(SDSS) with spectral energy distribution fitting using the Ultraviolet to midIR photometric data. Among the 50 galaxies from present sample, 39 were found to occupy the position of *"Blue-cloud"* and *"Green valley"* region in the CMD plane. We compute the parameters such as stellar mass, dust mass, dust luminosity, specific star formation rate and it's correlation with central black hole mass. This could depict a scenario suggesting ba two way migration of *"Green valley"* galaxies, either from SF phase to red sequence or from red sequence to the SF. Specific star formation rate is found to have a strong dependence on the gas content of galaxy over the average stellar age of galaxy population such that younger the stellar population of a galaxy, larger is the gas fraction and hence show high specific star formation rate. This suggests that the star formation in these ETGs may purely of intrinsic origin.

Keywords Keywords: galaxies: early type, galaxies: evolution, galaxies: star formation, optical spectroscopy, SED fitting.

I Introduction

Early-type galaxies (ellipticals and lenticulars together) were broadly characterized by their roundish shapes, featureless morphologies, red colours, total absence or very little content of the inter stellar medium (ISM), and very smooth distribution of stellar light and mass over the effective radius confined in a plane (Djorgovski and Davis, 1987). They were believed to be passively evolving stellar systems following a tight red sequence of the galaxy colour magnitude relation (Baldry et al., 2004). Due to the lack of the gas and dust, later acting as a catalyst for the star formation, these systems were devoid of star formation activities and hence were regarded as the fossils of galaxy evolutions. However, this scenario has changed drastically over the years. Particularly, multi-frequency photometric and spectroscopic observations and deep surveys of ETGs in recent years employing high-sensitivity instruments have revealed that several of the elliptical and even more lenticular galaxies host a substantial fraction of dust and gas

in all the known phases e.g., Goudfrooij et al. (1994); Marino et al. (2011); Patil et al. (2007); Kulkarni et al. (2014), sufficient enough to generate appreciable amount of star formation (Temi et al., 2009; Huang and Gu, 2009). Evidence regarding the existence of cold gas in this class of galaxies was provided by the thermal dust emission in IR regions. Polycyclic aromatic hydrocarbon (PAH) emission, characterizing starburst phase, is detected in a large fraction of ETGs spectra e.g. Panuzzo et al. (2011). Presence of ionized gas has been revealed through the H_α nebular line emission measurements (Phillips et al., 1986; Capetti and Baldi, 2011; Ge and Gu, 2012), where as presence of X-ray emitting extremely hot gas in nearly all the ETGs has been confirmed through the systematic imaging analysis employing high resolution data from *Chandra* X-ray observatory (Canizares et al., 1987; Kim and Fabbiano, 2010; Summers et al., 2004; Pinto et al., 2014; Vagshette et al., 2013; Patil et al., 2007). X-ray study of these systems has revealed that the hot gas is mostly associated with the cooling flow mechanism in cluster dominant galaxies, nuclear activity or shock waves created during the galaxy merger process. Thus, the past studies have confirmed that hot, warm and cold phases of the ISM in these galaxies are spatially associated with one another (Vagshette et al., 2012; Deshmukh et al., 2013), suggesting that all these components support the same physical processes related to the galaxian evolutions.

Another important activity, the ongoing star formation, in this class of galaxies make these quiescent ETGs as active candidates. Recent studies of these galaxies strongly support the rejuvenated stellar episodes in ETGs. (Kannappan et al., 2009; Yi et al., 2005; George and Zingade, 2015; Schawinski et al., 2014; Deshmukh et al., 2022) found ETGs to reside along the blue cloud sequence in the color-magnitude diagram with $(u - r) < 2.22$, a contradictory magnitude for ETGs (Strateva et al., 2001) supporting the star formation process in ETGs. This introduces the idea of regrowth of spirals from ETGs as a product of galaxy evolution (Wei et al., 2010). The color - magnitude diagram exhibits a bimodality providing an important way to separate the passively evolving red galaxies from the actively star-forming blue galaxies.

Past studies have demonstrated that the stellar mass in these red sequence galaxies is increasing over the last eight billion years (Bell et al., 2004; Faber et al., 2007; Brown et al., 2007; George and Zingade, 2015). This is probably due to the growth of the stellar mass of the galaxies. Several mechanisms have been introduced to address for the star formation processes in ETGs. Among them, gravitational interaction or merging of gas rich components is believed to be the most significant mechanism that can start star formation and even starburst activity in this class of galaxies (Barton et al., 2000; Kaviraj et al., 2009; George, 2017). Some internal processes within galaxy may cause starburst phase such as instabilities produced by bars and jets and the energy injection from winds and supernovae can produce star formation in ETGs (Dressel, 1988; Gaibler et al., 2012; McDonald et al., 2015). These processes result in the increase in stellar mass of ETGs by accreting more stars and gas and hence triggering star formation through out the galaxy. As a result, the blue spectral energy distribution of the host systems gets elevated and hence yield into the change in their position from red sequence to the blue cloud in the colour-magnitude diagram of the galaxies.

Knowing the star formation histories (SFHs) of galaxies is key to understand the formation and evolution scenario of a galaxy. One can easily determine the SFH of a galaxy by performing spectro-photometric study of individual stars in it and by obtaining colour-magnitude diagram (Tosi et al., 1991). However, in the case of distant galaxies it is quite impossible to resolve individual star and hence to trace the SFHs of their host. In such cases, photometric spectral

energy distribution (SED) modelling based on parametrized SFHs may provide a potential way to constrain the full SFH of a galaxy (Conroy, 2013). Due to the advantage of requiring shorter integration time relative to the spectroscopic method, broad-band photometric data available in the archives of survey telescopes can greatly help to carryout the SED fitting. As a result, several researchers have employed the multi-frequency data sets for performing the best-fit SED model and to recover the current star formation rate (SFR) of galaxies.

This paper reports the SED and star formation activities in a sample of 50 blue ETGs within local universe exhibiting optical emission line spectra. All these systems have redshifts in the range between $0 < z < 0.05$ with the median equal to 0.0274. The early-type morphology of these galaxies has been confirmed through the visual inspection. In addition to the visual inspection, several other methods are proposed to classify galaxies morphologically as early and late types, which includes the Hubble T parameter, ratio of P_{exp} to P_{dev}, u-r color, etc. This paper uses the criteria of concentration index C_r for their identification. Here, C_r is defined as the ratio of Petrosian radii ($C_r = r_{90}/r_{50}$) containing 90% and 50% of the total galaxian light, respectively, in the SDSS r band[1]. It is reported that the ETGs including E, S0 and Sa have $C_r >$ 2.63, while spirals and irregulars have $2.0 < C_r > 2.63$ (Strateva et al., 2001). All the galaxies from our present sample have C_r greater than 2.63, classifying them as the ETGs. This paper is arranged in the following way. Section refsection 2 describes data collection and detailed data analysis strategies. Results from the study are reported in Section III whereas Section IV summaries our work.Through out the paper we adopt a flat universe cosmology with $\Omega_M = 0.3$, Ω_Λ=0.7 and $H_0 = 70$ km s^{-1}.

II Data acquisition and analysis

As discussed above we have selected a sample of 50 ETGs for the present study based on the criteria that they show optical emission line spectra from within the local universe with redshift in the range $0 < z < 0.05$. Basic data of the sample galaxies is summarized in Table 1. In order to compute a reliable SEDs fitting and investigate the star formation processes in each of the galaxy we have made use of the archival data with wavelength coverage spanning from the ultraviolet to the far-infrared. For this purpose we concentrate on the instruments that span these wavelengths and have extensive sky coverage, These include: GALEX for the UV part, SDSS for the optical, 2MASS for the near-IR, WISE for the mid-IR and IRAS for the far-IR coverage. Details of the data sets with their acquisition are discussed below.

I Imaging data

I.1 Ultraviolet data

To cover the ultraviolet (UV) part of the SED of ETGs we use GR6 data release of the *Galaxy Evolution Explorer (GALEX)*, which covers about 25,000 deg^2 ($\sim$ 63%) of the sky region to a depth of about m$_{AB}$=20 mag when is used for the All Sky Imaging Survey (AIS) and of m$_{AB}$=25 for the Deep Imaging Survey (DIS) (Morrissey et al., 2007). The UV emission images are good tracers for the investigation of dust content and hence the star forming regions in the host galaxies and are useful to measure the shape of the radiation field that is modified

[1]www.sdss.org

Table 1. Basic data for sample galaxies.

Sr.No.	SDSS Id	RA(J2000) hh:mm:ss	DEC(J2000) dd:mm:ss	redshift	D Mpc	r_{fibre}/r_{50}	C_r	M_r	classification
a	b	c	d	e	f	g	h	i	
1	J003009.05-095711.7	00:30:09.00	-09:57:12	0.017	73.8	0.48	2.81	-19.66	SF
2	J003823.71+150222.4	00:38:23.70	15:02:22	0.018	78.2	0.20	3.57	-20.57	SF
3	J010358.74+151450.1	01:03:58.70	15:14:50	0.042	185.6	0.40	3.05	-21.29	SF
4	J012729.23-083315.4	01:27:29.20	-08:33:15	0.049	217.7	0.69	3.03	-22.00	SF
5	J022628.28+010937.7	02:26:28.30	01:09:38	0.005	21.5	0.13	2.63	-17.28	SF
6	J023247.42+004041.1	02:32:47.40	00:40:41	0.023	100.2	0.74	2.80	-19.26	SF
7	J030349.10-010613.4	03:03:49.10	-01:06:13	0.014	60.6	0.13	2.78	-20.89	AGN
8	J075912.37+533325.9	07:59:12.40	53:33:26	0.035	153.9	0.68	3.33	-20.88	SF
9	J080740.99+390015.2	08:07:41.00	39:00:15	0.023	100.2	0.43	3.77	-21.11	AGN
10	J081616.93+255827.9	08:16:16.90	25:58:28	0.042	185.6	0.96	3.04	-20.80	COMP
11	J082938.74+520434.8	08:29:38.70	52:04:35	0.006	25.8	0.46	3.03	-17.48	SF
12	J085139.06+570626.6	08:51:39.00	57:06:27	0.026	113.6	0.39	3.07	-20.07	SF
13	J085311.41+370806.5	08:53:11.40	37:08:06	0.05	222.3	0.55	2.89	-21.56	SF
14	J094150.95+121101.5	09:41:50.90	12:11:02	0.023	100.2	0.40	3.61	-20.18	SF
15	J094403.20+293634.0	09:44:03.20	29:36:34	0.017	73.8	0.52	2.93	-20.15	COMP
16	J094941.20+321315.9	09:49:41.20	32:13:16	0.005	21.5	0.32	2.99	-18.46	AGN
17	J095700.62+595808.0	09:57:00.60	59:58:08	0.031	135.9	0.77	3.32	-20.92	SF
18	J100351.88+592610.3	10:03:51.90	59:26:10	0.01	43.2	0.45	3.28	-19.32	SF
19	J100604.28+534253.4	10:06:04.30	53:42:53	0.044	194.8	0.94	3.12	-20.98	COMP
20	J101720.02+152920.9	10:17:20.00	15:29:21	0.033	144.9	0.63	2.89	-21.03	SF
21	J101912.56+635802.6	10:19:12.50	63:58:03	0.041	181.1	0.42	2.86	-21.91	AGN
22	J102158.91+645847.9	10:21:58.90	64:58:48	0.040	176.5	0.42	3.18	-21.16	SF
23	J103106.76+284747.9	10:31:06.80	28:47:48	0.005	21.5	0.26	2.70	-18.62	SF
24	J104549.80+273711.2	10:45:49.80	27:37:11	0.044	194.8	0.31	2.79	-22.37	SF
25	J105437.89+553945.7	10:54:37.90	55:39:46	0.048	213.1	0.48	2.82	-20.82	SF
26	J111349.74+093510.7	11:13:49.70	09:35:11	0.029	127	0.26	3.04	-22.15	AGN
27	J111632.33+284635.3	11:16:32.30	28:46:35	0.024	104.7	0.54	2.61	-19.46	SF
28	J111732.39+512553.8	11:17:32.30	51:25:53	0.009	38.8	0.41	3.04	-17.37	SF
29	J114556.60+501159.0	11:45:56.60	50:11:59	0.002	8.6	0.38	2.87	-17.57	SF
30	J114700.72-001739.2	11:47:00.70	-00:17:39	0.005	21.5	0.24	2.74	-17.44	SF
31	J115147.62+484059.2	11:51:47.60	48:40:59	0.003	12.9	0.20	3.03	-18.76	COMP
32	J120617.05+633819.0	12:06:17.00	63:38:19	0.040	176.5	0.48	2.70	-21.18	SF
33	J120823.52+000636.9	12:08:23.50	00:06:37	0.041	181.1	0.46	3.31	-21.48	SF
34	J121035.68+114538.9	12:10:35.70	11:45:39	0.004	17.4	9.47	2.68	-16.83	SF
35	J123502.64+662233.4	12:35:02.60	66:22:33	0.047	208.5	0.86	3.27	-21.64	SF
36	J124813.65-031958.2	12:48:13.60	-03:19:58	0.004	17.2	0.11	2.82	-20.06	SF
37	J125651.17+265355.9	12:56:51.10	26:53:56	0.021	91.4	0.27	2.65	-20.40	AGN
38	J125725.24+272416.4	12:57:25.20	27:24:17	0.016	69.4	0.53	2.66	-19.01	AGN
39	J125835.33+271552.8	12:58:35.30	27:15:53	0.025	09.1	0.33	2.81	-19.88	SF
40	J134747.70+111626.9	13:47:47.70	11:16:27	0.039	172.0	0.46	2.99	-21.19	SF
41	J140747.19+523809.7	14:07:47.20	52:38:10	0.044	194.8	0.50	2.98	-20.74	SF
42	J141433.22+404522.9	14:14:33.20	40:45:23	0.042	185.6	0.75	3.17	-20.84	SF
43	J143222.70+565108.3	14:32:22.70	56:51:08	0.043	190.2	0.45	3.11	-21.71	SF
44	J151809.64+254211.5	15:18:09.60	25:42:12	0.033	144.9	0.38	2.63	-20.66	SF
45	J155000.46+415811.1	15:50:00.50	41:58:11	0.034	149.4	0.43	2.75	-20.74	SF
46	J155335.56+321820.5	15:53:35.50	32:18:21	0.05	222.3	0.61	3.15	-21.02	SF
47	J160753.98+200303.7	16:07:54.00	20:03:04	0.032	140.4	0.54	3.77	-20.66	SF
48	J164430.75+195626.7	16:44:30.70	19:56:27	0.023	100.2	0.37	3.02	-20.64	SF
49	J172324.87+274846.3	17:23:24.90	27:48:46	0.048	213.1	0.65	2.99	-21.38	SF
50	J221516.18-091547.6	22:15:16.20	-09:15:48	0.038	167.5	0.35	3.00	-21.48	SF

due to the presence of PAHs. GALEX is a NASA's Small explorer mission equipped with two microchannel plate imaging detectors working in the near-UV (NUV) at 2267 $\mathring{A}$ and far-UV (FUV) at 1516 $\mathring{A}$ and a grism to perform low resolution slit less spectroscopy (Morrissey et al., 2007). Angular resolutions of FUV and NUV are 4.25 and 5.25 arcseconds, respectively, with the source position accuracy of 0.34 arcseconds. As GALEX imaging surveys include different modes i.e., AIS, MIS, DIS and NGS, therefore exposure time and sensitivity limits are different for different surveys. Mission survey data sets are available to public via the Multi-mission Archive at Space Telescope Science Institute (MAST)[2]. Out of the sample of 50 galaxies we find GALEX AIS data for 37 in FUV and NUV bands. FUV and NUV apparent magnitudes were calibrated through the GALEX pipeline using SExtractor code in the AB magnitude system defined by Oke and Gunn (1983). These apparent UV magnitudes were corrected for the galactic dust extinction E(B-V) obtained using Schlegel et al. (1998) reddening maps and assuming the extinction law of Cardelli et al. (1989). We assume the Milky Way dust with $R_V = 3.1$ and apply the dust extinction corrections to the GALEX data using relations A_{FUV}/E(B-V) = 8.376 and A_{NUV}/E(B-V) = 8.741 (Marino et al., 2011).

[2]https://archive.stsci.edu/

I.2 Optical observations

We have used seventh data release (DR7) of the Sloan Digital Sky Survey (SDSS, Abazajian et al. (2009)), which is an ambitious astronomical survey release in the imaging and spectroscopic mode acquired using a 2.5m optical telescope at Apachi Point Observatory at New Mexico, to cover the optical region of the SED of our program galaxies. Te SDSS covers a large region of the sky (about 14,555 deg^2) with an angular resolution of about 1.5 arcseconds. The SDSS photometric data is measured almost simultaneously in five different bands namely, u, g r, i and z with respective effective wavelengths of 3543, 4770, 6231, 7625, and 9134 $\mathring{A}$. The telescope is also equipped with a double 3 arcsec diameter Fiber-fed pair spectrograph that covers wavelength range of 3800$\mathring{A}$ to 9200$\mathring{A}$ at a resolution of 2000. SDSS provides wavelength and flux calibrated spectra of a fairly large number of astronomical objects including stars AGNs, Quasars, SF galaxies covering a wide range of redshift enabling us to determine various physical properties such as redshift, velocity dispersion, star formation rate, metallicity and several other. All the 50 galaxies in our sample have SDSS photometric and spectroscopic data. We considered the Petrosian magnitudes for the sample galaxies that consider galaxy fluxes within a circular aperture whose radius is defined by the shape of the azimuthally averaged light profile and hence approximately represent the total galaxy flux. SDSS magnitudes are Vega magnitudes. SDSS g, r and i band magnitudes are close to AB magnitudes and that of the u and z band were converted to their equivalent AB magnitudes following relations $u_{AB} = u_{SDSS} - 0.04$ and z_{AB}=z_{SDSS}+0.02. The SDSS r band imagery of the program galaxies is shown in Figure 1.

I.3 Infrared data

To cover the IR part of the spectral energy distribution, we have made use of the Two Micron All Sky Survey (2MASS) Extended source catalog (EXC) (Skrutskie et al., 2006) for near IR (JHKs) data, The wide-field Infrared Survey (WISE) (Wright et al., 2010) for mid-IR data and Infrared Astronomical Satellite (IRAS) faint source catalog data for the far-IR observations of the sample galaxies. We considered Ks fiducial elliptical aperture JHKs band magnitude of sample galaxies from 2MASS survey. WISE satellite has observed the entire sky in four mid-IR bands: W1 (3.4μm), W2 (4.6μm), W3(12μm), and W4 (22μm). The first two bands W1 and W2 are identical to the *Spitzer* IR Array Camera bands, while W4 is identical to the Multiband Imaging Photometer 24μm band of *Spitzer*. For the case of galaxies W1 and W2 will help us to trace the evolved stellar population, while W3 and W4 help us to understand the PAH emission characteristics and continuum emission from the dust grains, respectively (Jarrett et al., 2013). This all-sky survey capability of WISE has enabled us to get sufficient quality data on nearly all the bright ETGs and hence provided us with a valuable demographic information regarding the stellar populations, circumstellar dust, and PAHs. For the present study we have made use of the *Allwise* catalog of WISE survey data considering $w - g$ magnitudes extracted from the apertures scaled from 2MASS EXC shape values and hence represent total integrated flux of galaxy. The IRAS datasets on our sample enabled us to better constrain the peak of the SED in the IR and also to derive the temperature of the dust content of the sources. We obtain the IRAS fluxes and errors in the 2 IRAS bands namely 60 and 100 μm taking into account that for most of our program galaxies, the quality flag for IRAS 12 and 25μm filter was not considerable.The IRAS datasets on sample galaxies are useful to better constrain the peak of the SEDs in the IR and also to derive the temperature of the dust grains in the galaxies.

GALEX and SDSS magnitudes were k corrected using k-correction calculator of Chilingarian and Zolotukhin (2012). As 2MASS, WISE and IRAS employ the wide band filters, therefore, the k-correction for sample galaxies with redshift $0 \leq z \leq 0.05$ is not required. Further, GALEX magnitudes resulting from the code *SEXtractor*, SDSS petrosian magnitudes, 2MASS Ks isophotal fiducial elliptical aperture magnitudes and corresponding *AllWISE* magnitudes represent the total galaxian fluxes, therefore, we have not applied aperture correction. The flux values derived in this way are used for further analysis and are as listed in Table 2 and Table 3.

Table 2. MAGPHYS input flux values from GALEX and SDSS. Fluxes are retrieved as discussed in section 2.

SDSS Id	FUV	NUV	u	g	r	i	z
	Jy	Jy	mJy	mJy	mJy	mJy	mJy
J003009.05-095711.7	287.38±7.86	500.00 ±13.68	1.33±0.03	3.64 ±0.05	5.54 ±0.07	7.83 ±0.10	9.31 ±0.13
J003823.71+150222.4	-	-	1.95±0.06	6.88±0.07	12.20 ±0.16	18.30± 0.18	18.60± 0.36
J010358.74+151450.1	-	-	0.60± 0.02	2.25± 0.02	4.00± 0.04	6.12± 0.06	7.36± 0.09
J012729.23-083315.4	68.46± 9.92	199.35± 10.73	0.95± 0.02	3.28± 0.03	5.37± 0.05	8.31± 0.07	10.38± 0.11
J022628.28+010937.7	506.69± 23.00	781.96± 21.87	1.52± 0.05	5.82± 0.06	8.80± 0.08	12.14± 0.11	12.13± 0.17
J023247.42+004041.1	946.34± 12.80	1147.98± 11.95	1.36± 0.02	1.95± 0.02	2.06± 0.02	2.24± 0.03	2.35± 0.04
J030349.10-010613.4	44.11± 4.62	224.70± 14.07	1.73± 0.06	12.72± 0.11	28.10± 0.26	43.03± 0.39	52.82± 0.51
J075912.37+533325.9	-	-	0.80± 0.02	2.35± 0.02	3.47± 0.04	5.20± 0.05	6.05± 0.07
J080740.99+390015.2	142.60± 12.57	388.51± 14.26	1.76± 0.03	6.01± 0.06	9.59± 0.09	14.14± 0.13	16.60± 0.18
J081616.93+255827.9	71.10± 6.85	223.33± 8.09	0.65± 0.01	1.49± 0.01	2.00± 0.02	3.24± 0.03	3.82± 0.05
J082938.74+520434.8	706.90± 20.14	954.81± 19.32	1.76± 0.03	3.84± 0.04	5.19± 0.06	6.11± 0.07	6.66± 0.09
J085139.06+570626.6	101.11± 12.31	183.74± 11.78	0.65± 0.03	1.94± 0.02	3.13± 0.03	4.57± 0.05	5.45± 0.10
J085311.41+370806.5	-	-	0.57± 0.02	1.86± 0.03	3.29± 0.06	4.94± 0.08	5.98± 0.11
J094150.95+121101.5	247.37± 17.70	484.11± 18.09	1.11± 0.02	2.80± 0.03	4.09± 0.05	5.67± 0.06	6.38± 0.08
J094403.20+293634.0	-	-	1.50± 0.03	4.45± 0.04	7.48± 0.06	10.50± 0.09	12.74± 0.13
J094941.20+321315.9	777.78± 21.40	1040.21± 19.43	2.71± 0.04	8.50± 0.08	14.08± 0.13	19.53± 0.18	22.59± 0.22
J095700.62+595808.0	180.24± 14.34	381.92± 13.82	1.03± 0.02	2.89± 0.04	4.67± 0.06	6.81± 0.09	8.25± 0.11
J100351.88+592610.3	850.12± 30.81	1340.70± 24.68	2.77± 0.04	6.31± 0.06	9.45± 0.09	13.44± 0.14	15.59± 0.17
J100604.28+534253.4	130.83± 11.53	221.64± 10.03	0.57± 0.01	1.50± 0.01	2.28± 0.02	3.50± 0.03	4.29± 0.05
J101720.02+152920.9	331.84± 15.14	628.91± 12.52	1.49± 0.02	3.29± 0.03	4.46± 0.05	6.03± 0.06	7.05± 0.09
J101912.56+635802.6	464.97± 20.93	795.87± 21.70	1.83± 0.03	4.13± 0.04	5.97± 0.05	9.42± 0.08	11.01± 0.12
J102158.91+645847.9	-	-	0.83± 0.02	2.26± 0.02	3.43± 0.03	4.98± 0.05	5.75± 0.09
J103106.76+284747.9	521.59± 14.26	1088.29± 20.03	3.53± 0.05	11.30± 0.10	18.86± 0.51	29.42± 0.49	32.97± 0.31
J104549.80+273711.2	536.67± 24.36	949.48± 18.35	1.87± 0.03	5.54± 0.05	7.99± 0.08	11.06± 0.10	10.98± 0.13
J105437.89+553945.7	-	-	0.33± 0.01	1.09± 0.01	1.80± 0.02	2.68± 0.03	3.17± 0.06
J111349.74+093510.7	440.18± 23.70	892.89± 24.50	2.96± 0.05	9.66± 0.08	15.11± 0.13	22.72± 0.19	26.04± 0.27
J111632.33+284635.3	15.07± 5.56	88.84± 5.56	0.39± 0.01	1.33± 0.01	1.98± 0.02	2.79± 0.03	3.16± 0.05
J111732.39+512553.8	163.39± 13.01	288.25± 13.00	0.61± 0.02	1.28± 0.02	1.65± 0.03	2.09± 0.04	2.15± 0.06
J114556.60+501159.0	3063.30± 55.96	4172.76± 38.40	7.25± 0.10	15.93± 0.14	21.58± 0.21	27.79± 0.28	29.72± 0.29
J114700.72-001739.2	422.77± 8.77	617.19± 8.54	1.41± 0.04	3.50± 0.03	5.17± 0.05	7.02± 0.07	7.29± 0.11
J115147.62+484059.2	2279.90± 42.51	3703.91± 37.04	7.48± 0.11	24.48± 0.21	42.32± 0.36	58.39± 0.49	66.50± 0.63
J120617.05+633819.0	76.08± 8.58	185.86± 5.07	0.72± 0.02	2.20± 0.02	3.46± 0.03	5.53± 0.05	6.64± 0.07
J120823.52+000636.9	85.24± 10.33	191.32± 10.37	0.81± 0.02	2.71± 0.02	4.45± 0.04	6.45± 0.06	7.84± 0.09
J121035.68+114538.9	205.71± 11.07	335.10± 12.15	1.01± 0.02	2.62± 0.02	3.86± 0.04	4.98± 0.05	5.47± 0.08
J123502.64+662233.4	74.00± 10.74	172.66± 9.38	0.71± 0.02	2.42± 0.05	3.99± 0.08	5.82± 0.12	7.09± 0.15
J124813.65-031958.2	11642.84± 44.82	19862.34± 79.79	22.40± 0.50	63.16± 0.93	92.81± 1.44	127.23± 2.27	132.81± 1.46
J125651.17+265355.9	-	-	1.08± 0.02	3.75± 0.03	6.28± 0.05	9.16± 0.08	10.24± 0.12
J125725.24+272416.4	-	-	0.70± 0.02	1.77± 0.02	2.70± 0.04	3.78± 0.06	4.50± 0.07
J125835.33+271552.8	326.9±5 2.51	483.48± 3.88	0.95± 0.02	2.18± 0.02	2.63± 0.02	3.27± 0.03	3.58± 0.08
J134747.70+111626.9	-	-	0.71± 0.02	2.28± 0.02	3.67± 0.04	5.12± 0.06	6.10± 0.08
J140747.19+523809.7	-	-	0.41± 0.01	1.29± 0.01	2.00± 0.02	2.84± 0.03	3.35± 0.05
J141433.22+404522.9	-	-	0.56± 0.01	1.47± 0.02	2.32± 0.04	3.47± 0.05	4.33± 0.07
J143222.70+565108.3	116.21± 11.20	233.98± 10.53	0.90± 0.02	3.02± 0.03	5.11± 0.04	7.56± 0.06	8.83± 0.09
J151809.64+254211.5	49.35± 5.16	92.30± 4.15	0.50± 0.02	1.93± 0.02	3.31± 0.03	5.16± 0.05	6.06± 0.08
J155000.46+415811.1	81.89± 9.24	144.94± 7.79	0.65± 0.02	2.03± 0.02	3.43± 0.03	5.03± 0.04	6.14± 0.07
J155335.56+321820.5	75.38± 8.51	87.33± 3.93	0.42± 0.01	1.30± 0.01	1.96± 0.02	2.85± 0.03	3.37± 0.05
J160753.98+200303.7	116.21± 8.25	215.37± 5.87	0.90± 0.02	2.38± 0.02	3.54± 0.03	5.17± 0.05	6.04± 0.08
J164430.75+195626.7	57.71± 5.56	167.95± 7.56	1.22± 0.02	4.15± 0.04	6.76± 0.06	10.12± 0.09	12.19± 0.13
J172324.87+274846.3	46.69± 5.27	101.20± 6.32	0.61± 0.01	1.93± 0.02	3.00± 0.03	4.42± 0.04	5.27± 0.06
J221516.18-091547.6	-	-	1.04± 0.03	3.32± 0.03	5.29± 0.05	8.22± 0.08	9.75± 0.12

II Spectroscopic data

We have also made use of the SDSS DR7 spectral data of the sample galaxies for fitting the SED. The acquired spectra on these galaxies were reduced using the software package IRAF (Image Reduction and Analysis Facility). All the spectra were converted to the rest frame using the task *dopcor* and were also corrected for the Galactic extinction using task *deredden* follow-

Table 3. MAGPHYS input flux values from 2MASS,WISE AND IRAS. Fluxes are retrieved as discussed in section 2.

SDSS Id	J	H	Ks	w1	w2	w3	w4	60m	100 m
	mJy	mJy	mJy	mJy	mJy	mJy	mJy	Jy	Jy
J003009.05-095711.7	10.50 ±0.29	12.40 ±0.48	9.74 ±0.57	5.14 ±0.03	3.12 ±0.02	12.94 ±0.12	36.97±0.84	0.67±0.06	0.93±0.17
J003823.71+150222.4	22.90±0.58	27.70 ±1.10	23.30 ± 1.19	11.75 ± 0.06	7.07±0.05	27.03 ± 0.20	37.17 ±1.18	0.73 ± 0.07	1.27±0.23
J010358.74+151450.1	8.78± 0.34	11.20± 0.45	10.40± 0.77	5.29± 0.03	3.29± 0.03	11.60± 0.11	11.67± 0.70	-	-
J012729.23-083315.4	15.70± 0.31	19.90± 0.56	19.80± 0.73	11.28± 0.06	8.74± 0.05	61.53± 0.34	139.51± 1.15	3.60± 0.25	6.82± 0.41
J022628.28+010937.7	9.83± 0.43	9.33± 0.66	7.03± 0.68	4.87± 0.03	2.73± 0.03	5.28± 0.14	10.96± 0.71	-	-
J023247.42+004041.1	1.95± 0.11	1.84± 0.14	1.82± 0.18	0.88± 0.02	0.53± 0.02	1.90± 0.12	12.39± 0.78	-	-
J030349.10-010613.4	73.00± 1.27	83.10± 2.12	75.60± 2.20	55.76± 0.26	81.32± 0.45	195.12± 1.08	400.87± 2.58	0.77± x	0.93± y
J075912.37+533325.9	6.91± 0.23	8.31± 0.37	7.38± 0.38	-	-	-	-	0.81± 0.06	1.01± 0.16
J080740.99+390015.2	19.20± 0.57	23.00± 0.89	19.60± 0.90	13.11± 0.07	11.72± 0.06	60.35± 0.33	214.88± 1.38	1.28± x	1.43± y
J081616.93+255827.9	5.13± 0.15	6.17± 0.21	5.76± 0.26	3.14± 0.03	2.45± 0.02	25.37± 0.19	126.65± 0.93	1.18± 0.07	1.27± 0.15
J082938.74+520434.8	6.40± 0.21	6.97± 0.28	5.88± 0.36	2.78± 0.02	1.64± 0.02	3.97± 0.12	12.72± 0.90	0.26± 0.04	0.67± z
J085139.06+570626.6	5.23± 0.21	6.33± 0.33	5.37± 0.32	2.78± 0.02	1.66± 0.02	4.76± 0.10	8.57± 0.69	-	-
J085311.41+370806.5	7.84± 0.22	9.63± 0.37	8.82± 0.40	4.42± 0.03	2.76± 0.03	9.52± 0.12	12.45± 0.81	0.35± 0.04	0.78± 0.15
J094150.95+121101.5	5.68± 0.24	6.60± 0.35	5.54± 0.40	3.07± 0.02	1.89± 0.02	8.66± 0.10	21.08± 0.65	0.37± 0.05	0.62± 0.16
J094403.20+293634.0	14.80± 0.39	17.10± 0.57	14.20± 0.73	6.28± 0.03	3.49± 0.03	6.29± 0.10	6.82± 0.66	0.24± 0.04	
J094941.20+321315.9	23.20± 0.38	25.50± 0.58	20.50± 0.67	10.30± 0.06	5.71± 0.04	9.73± 0.17	11.70± 0.88	0.23± 0.04	0.61± 0.12
J095700.62+595808.0	12.20± 0.44	14.60± 0.73	13.40± 0.79	6.43± 0.04	4.00± 0.03	16.62± 0.11	31.84± 0.58	0.57± 0.05	0.69± 0.15
J100351.88+592610.3	18.50± 0.37	21.80± 0.52	18.50± 0.73	9.75± 0.05	6.00± 0.04	35.38± 0.23	126.42± 0.93	1.25± 0.07	1.59± 0.16
J100604.28+534253.4	5.07± 0.19	6.31± 0.30	5.75± 0.32	-	-	-	-	-	-
J101720.02+152920.9	7.97± 0.22	9.60± 0.38	8.71± 0.38	5.05± 0.03	3.53± 0.03	23.74± 0.15	44.90± 1.06	0.94± 0.08	1.58± 0.17
J101912.56+635802.6	13.80± 0.44	17.30± 0.76	18.40± 0.86	11.75± 0.06	13.07± 0.07	41.52± 0.23	87.54± 0.96	-	-
J102158.91+645847.9	6.38± 0.32	7.38± 0.52	7.19± 0.54	3.21± 0.02	1.95± 0.02	7.63± 0.10	8.94± 0.50	-	-
J103106.76+284747.9	41.50± 0.64	50.00± 0.78	41.40± 0.76	21.93± 0.12	13.57± 0.09	71.50± 0.39	182.90± 1.51	2.18± 0.17	3.39± 0.20
J104549.80+273711.2	15.80± 0.50	18.00± 0.78	18.20± 1.09	9.57± 0.05	7.03± 0.05	48.65± 0.31	145.82± 1.20	1.81± 0.11	2.86± 0.20
J105437.89+553945.7	3.83± 0.17	4.47± 0.28	4.10± 0.26	-	-	-	-	-	-
J111349.74+093510.7	33.90± 0.89	42.20± 1.30	38.20± 1.85	25.28± 0.14	19.20± 0.11	94.17± 0.52	121.06± 1.22	-	-
J111632.33+284635.3	3.55± 0.15	4.11± 0.20	3.88± 0.25	-	-	-	-	-	-
J111732.39+512553.8	1.16± 0.10	1.39± 0.15	0.85± 0.14	-	-	-	-	-	-
J114556.60+501159.0	32.00± 0.64	35.90± 1.27	27.30± 1.23	15.88± 0.09	9.55± 0.06	32.89± 0.24	67.33± 1.23	1.09± 0.07	2.52± 0.18
J114700.72-001739.2	4.74± 0.23	5.51± 0.31	3.75± 0.41	2.16± 0.02	1.20± 0.02	1.44± 0.10	4.11± 0.75	-	-
J115147.62+484059.2	83.90± 1.30	98.30± 2.24	80.60± 1.98	44.41± 0.24	26.98± 0.15	141.09± 0.78	266.81± 1.96	2.80± 0.11	5.07± 0.25
J120617.05+633819.0	8.70± 0.25	10.40± 0.40	10.10± 0.53	5.44± 0.03	3.71± 0.02	22.24± 0.14	52.02± 0.57	-	-
J120823.52+000636.9	8.42± 0.33	10.70± 0.45	8.64± 0.61	4.10± 0.02	2.35± 0.02	5.84± 0.11	5.45± 0.76	-	-
J121035.68+114538.9	5.13± 0.33	6.13± 0.47	5.32± 0.58	2.00± 0.01	1.11± 0.02	1.00± 0.09	0.92± 0.52	-	-
J123502.64+662233.4	9.57± 0.24	11.80± 0.36	10.40± 0.44	5.32± 0.03	3.31± 0.02	10.00± 0.08	17.74± 0.67	-	-
J124813.65-031958.2	254.00± 3.25	288.00± 4.47	231.00± 5.88	-	-	-	-	14.73± 0.88	20.59± 2.06
J125651.17+265355.9	12.10± 0.32	14.70± 0.52	12.40± 0.60	5.94± 0.03	3.87± 0.03	13.76± 0.13	17.97± 1.18	-	-
J125725.24+272416.4	4.64± 0.18	5.43± 0.28	4.71± 0.28	-	-	-	-	-	-
J125835.33+271552.8	2.52± 0.12	2.27± 0.17	2.21± 0.17	-	-	-	-	-	-
J134747.70+111626.9	7.11± 0.30	8.56± 0.42	6.94± 0.55	3.80± 0.02	2.38± 0.02	10.77± 0.11	11.46± 0.64	0.26± 0.07	0.87± 0.17
J140747.19+523809.7	3.52± 0.22	4.32± 0.29	4.50± 0.43	2.28± 0.02	1.48± 0.02	7.36± 0.12	8.04± 0.55	0.20± 0.03	0.61± 0.12
J141433.22+404522.9	4.99± 0.18	6.19± 0.27	5.56± 0.34	2.39± 0.02	1.39± 0.01	3.01± 0.06	8.95± 0.48	0.36± 0.08	-
J143222.70+565108.3	11.00± 0.34	14.40± 0.58	11.20± 0.59	5.70± 0.03	3.36± 0.02	8.48± 0.08	11.46± 0.50	0.26± 0.03	0.61± 0.12
J151809.64+254211.5	7.74± 0.26	10.00± 0.44	8.41± 0.42	4.16± 0.02	2.60± 0.03	9.58± 0.08	25.18± 0.62	0.36± 0.04	-
J155000.46+415811.1	7.49± 0.28	9.21± 0.47	8.11± 0.44	3.87± 0.02	2.37± 0.02	9.88± 0.08	10.82± 0.41	0.23± 0.03	0.58± 0.16
J155335.56+321820.5	3.34± 0.17	3.91± 0.26	3.35± 0.27	1.60± 0.01	0.94± 0.02	2.38± 0.05	4.32± 0.37	-	-
J160753.98+200303.7	6.18± 0.26	7.19± 0.46	6.14± 0.43	2.96± 0.02	1.75± 0.02	5.21± 0.09	11.48± 0.69	0.24± 0.04	-
J164430.75+195626.7	13.30± 0.37	17.50± 0.60	14.80± 0.63	7.12± 0.04	4.40± 0.03	20.04± 0.15	25.74± 0.77	0.26± 0.07	0.87± 0.17
J172324.87+274846.3	6.25± 0.23	7.40± 0.37	6.38± 0.35	3.22± 0.02	1.95± 0.02	6.69± 0.06	6.95± 0.39	0.19± 0.03	-
J221516.18-091547.6	11.00± 0.37	13.30± 0.62	12.00± 0.77	5.80± 0.04	3.68± 0.03	12.82 0.18	39.07 1.03	0.53 0.05	-

ing the same process as discussed above. In order to calculate equivalent widths and integrated flux values of emission lines we used *deblending* program provided in SPLOT package of IRAF, which allows an interactive approach to fit Gaussian profiles to the observed asymmetric emission lines. Computed integrated flux values were then required to be calibrated by applying few corrections onto them.

II.1 Stellar absorption correction

Emission line fluxes calculated above normally provide underestimated values due to the effect of underlying stellar absorption and is significantly large in the case of H_β, H_γ and H_δ emission lines. To remove effect of the underlying stellar absorption we first fit a Gaussian profile to the emission line, quantified the corresponding flux values and then subtracted the modeled emission line from the original spectrum. The resulting absorption line was fitted with respect to the continuum. Then following the procedure outlined by (Kong et al., 2002) we

measured the stellar absorption corrected flux value for each of the line using relation

$$F_{int} = F_{obs}\left(1 + \frac{EW_{abs}}{EW_{obs}}\right) \tag{1}$$

where, F_{int} and F_{obs} represent the intrinsic, stellar absorption corrected galactic extinction corrected emission line flux and the observed emission line flux values, respectively, while EW_{abs} and EW_{obs} represent the equivalent widths of the underlying stellar absorption and observed emission lines, respectively.

II.2 Internal extinction correction

The interstellar dust present within the program galaxy also modifies the observed spectra by causing their extinction. As a result, it is required to correct the observed emission line flux values to overcome the internal reddening effect. Widely used method for correcting the emission line flux values due to the presence of internal dust relies on the measurement of relative strengths of low order Balmer emission line ratios e.g. H_α/H_β, H_γ/H_β, H_δ/H_β. The intrinsic Balmer line ratio H_α/H_β for the star forming galaxy is 2.86 (Osterbrock and Ferland, 2006) and assume case B recombination process with electron density and temperature values equal to 100 cm^{-3} and 10,000 K, respectively. We used the same value of the ratio of Balmer lines to compensate for the internal dust modification. The intrinsic flux density f_{int} at wavelength λ is obtained from the observed flux density $f_{obs}(\lambda)$ though the equation (Calzetti et al., 2000)

$$f_{int}(\lambda) = f_{obs}(\lambda)10^{0.4A_\lambda} \tag{2}$$

where, attenuation A_λ is related with the total to selective extinction through the relation $R_V = \frac{A_\lambda}{E(B-V)}$. The intrinsic color excess due to the internal dust attenuation can be expressed as

$$A(H_\beta) - A(H_\alpha) = E(H_\beta - H_\alpha) = -2.5\log_{10}\left[\frac{(H_\alpha/H_\beta)_{int}}{(H_\alpha/H_\beta)_{obs}}\right] \tag{3}$$

here, $\left(\frac{H_\alpha}{H_\beta}\right)_{int}$ and $\left(\frac{H_\alpha}{H_\beta}\right)_{obs}$, respectively, represent the intrinsic and observed emission line flux ratios. The intrinsic excess color thus derived can be related with the broadband color excess E(B-V) through the attenuation curve as $A(\lambda) = \kappa(\lambda)E(B-V)$, where, $\kappa(\lambda)$ specifies the attenuation curve at wavelength λ . This equation is also expressed as

$$E(H_\beta - H_\alpha) = [\kappa(H_\beta) - \kappa(H_\alpha)]E(B-V) \tag{4}$$

For this purpose we adopt (Calzetti, 1997) attenuation curve in the form

$$\kappa(\lambda) = 2.659(-1.857 + 1.040x) + R_V, \qquad \text{for} \quad 0.63m < \lambda < 2.20m \tag{5}$$

$$\kappa(\lambda) = 2.659(-2.156 + 1.509x - 0.198x^2 + 0.011x^3) + R_V, \qquad \text{for } 0.12m < \lambda < 0.63m \tag{6}$$

where, $x(= \lambda^{-1})$ represents the wave number and R_V the ratio of total to selective absorption and is taken to be equal to 3.1 like that for the Milky Way. Following these equations we obtain $\kappa(H_\beta)$ = 3.64 and $\kappa(H_\alpha)$ =2.376. These values were then used to obtain the broadband color excess as

$$E(B-V) = \frac{E(H_\beta - H_\alpha)}{\kappa(H_\beta) - \kappa(H_\alpha)} = \frac{-2.5}{\kappa(H_\beta) - \kappa(H_\alpha)}\log\left[\frac{2.86}{(H_\alpha/H_\beta)_{obs}}\right] \tag{7}$$

We use these color excess values to calculate corresponding dust attenuation and hence the intrinsic flux density of H_α emission line for each of the galaxy. This flux density was then employed for estimating star formation rates in the program galaxies.

II.3 Aperture correction

The SDSS spectra acquired using 3" diameter fiber detects a limited amount of emission from a galaxy therefore, in addition to the internal extinction correction and the stellar absorption correction we have to apply an aperture correction to them so as to derive the true emission line luminosities. This is particularly important for the case of nearby galaxies, while that for the distant galaxies it may provide the integrated spectrum. The fraction of galaxy size that has been covered by the SDSS fiber for each of the system from our sample is given in column f of Table 1. To obtain the integrated emission line flux from the entire galaxy we have applied the aperture correction to the measured emission line flux values following the method suggested by Hopkins et al. (2003) using the ratio of the fluxes corresponding to the total galaxy magnitude and the magnitude measured through the fiber. While adopting this aperture correction method, we are used to suppose that star formation is uniform through out the galaxy. In case of patchy distribution of star formation, this method may add uncertainty. The extent of the aperture correction for $H\alpha$ emission line flux was given by

$$A = 10^{-0.4(r_{petro} - r_{fiber})}$$

where, r_{petro} and r_{fibre} represent the r band Petrosian and fiber magnitudes, respectively. This aperture-corrected H_α luminosity was thus obtained using relation

$$L_{H\alpha} = 4\pi D_l^2 S_{H\alpha} 10^{-0.4(r_{Petro} - r_{fiber})} \text{ Watts} \quad (8)$$

where, $S_{H\alpha}$ representing the stellar absorption-corrected flux of the H_α emission and D_l the luminosity distance.The resultant flux densities of emission lines after correcting for various effects discussed above are listed in Table 3.

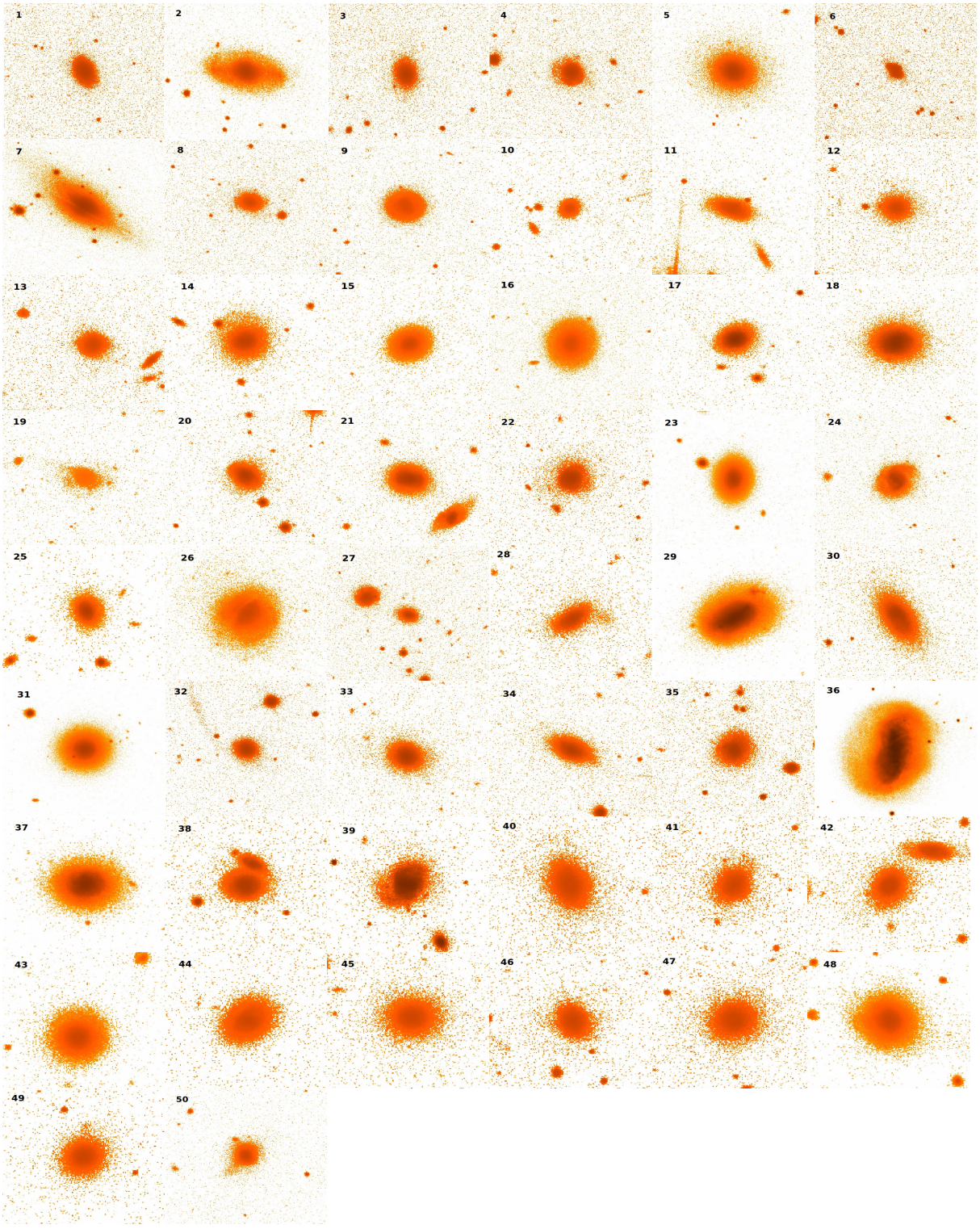

Figure 1. SDSS r band images of program galaxies.

III Results and Discussion

I BPT diagram

Though the star forming galaxies from among the sample for the present study have been identified above, in few of the analogy that the SFR is likely be influenced by the nuclear activity at the core of the host, we separate AGNs from the normal star forming galaxies using the classical BPT diagram. For this purpose we make use of the optical line flux ratios. For e.g.,Ratio of the optical lines $[OIII]\lambda5007/H_\beta\lambda4861$ is a good tracer of the degree of ionization and temperature of emitting gas compared to that of $[NII]\lambda6583/H\alpha\lambda6563$, where the latter is sensitive to the lines originating from the partially ionized gas due to a high energy sources like OB associations, while both these line flux ratios takes larger values for the case where the emission is originating from AGNs.

Table 3. Spectroscopic data for program galaxies.

SDSS Id	Observed emission line flux(10^{-17} egr/s/cm^2)						
	$H\beta\lambda$ 4861Å[3]	$[OII]\lambda$ 5007Å	$H\alpha\lambda$ 6563Å	[NII]λ 6584Å	EW(Hα)	$L_{H\alpha}(10^{41}$ erg/s)[4]	$SFR_{H\alpha flux}$
a	b	c	d	e	f	g	h
J003009.05-095711.7	1883	1021	6231	2223	58.69	2.624	1.25
J003823.71+150222.4	1511	0301	3509	1704	25.38	1.315	0.62
J010358.74+151450.1	0547	0031	1169	0516	13.59	1.418	0.67
J012729.23-083315.4	1210	0224	5564	2910	33.30	25.024	11.91
J022628.28+010937.7	1308	0988	4280	0911	87.67	0.491	0.23
J023247.42+004041.1	1748	7745	5563	0329	93.91	2.558	1.21
J075912.37+533325.9	2026	0383	7186	3048	67.92	10.383	4.94
J082938.74+520434.8	2059	4411	4766	0530	47.33	0.127	0.06
J085139.06+570626.6	1101	0201	3226	1467	44.75	2.380	1.13
J085311.41+370806.5	0433	0075	1486	0624	19.64	5.596	2.66
J094150.95+121101.5	1782	0460	5071	1716	61.56	2.731	1.30
J095700.62+595808.0	2209	0428	6491	3026	39.24	4.595	2.19
J100351.88+592610.3	6195	5561	21561	7257	107.90	3.151	1.50
J101720.02+152920.9	1903	0705	6794	2227	64.25	10.784	5.13
J102158.91+645847.9	0844	0294	2352	1090	37.64	4.844	2.30
J103106.76+284747.9	4535	1487	16871	6908	72.76	1.343	0.64
J104549.80+273711.2	2732	0676	9621	5133	69.52	37.822	18.01
J105437.89+553945.7	0254	0060	0939	0301	26.05	4.358	2.07
J111632.33+284635.3	0663	0436	2329	0695	54.05	2.086	0.99
J111732.39+512553.8	1476	5963	4660	0292	198.20	0.637	0.30
J114556.60+501159.0	4704	7137	12502	1765	68.93	0.109	0.05
J114700.72-001739.2	0674	1394	1965	0205	55.84	0.141	0.06
J120617.05+633819.0	1099	0181	4524	2033	65.67	18.349	8.73
J120823.52+000636.9	0668	0107	1108	0552	11.63	0.745	0.35
J121035.68+114538.9	0464	0510	0786	0096	16.62	0.008	0.004
J123502.64+662233.4	1219	0152	2596	1480	17.42	2.096	0.99
J124813.65-031958.2	4951	2313	15320	5698	58.36	2.061	0.98
J125835.33+271552.8	0757	0453	2544	0587	85.99	4.071	1.93
J134747.70+111626.9	0689	0106	1478	0658	19.75	1.540	0.73
J140747.19+523809.7	0414	0058	1132	0402	27.58	2.313	1.10
J141433.22+404522.9	1338	1430	3829	1119	48.22	4.990	2.37
J143222.70+565108.3	0657	0080	1783	0798	19.50	3.904	1.85
J151809.64+254211.5	0608	0108	2329	1204	33.22	5.602	2.66
J155000.46+415811.1	0481	0076	1318	0536	21.86	1.931	0.92
J155335.56+321820.5	0503	0196	1208	0480	24.32	1.897	0.90
J160753.98+200303.7	1763	1002	5075	1751	51.65	4.516	2.15
J164430.75+195626.7	1510	0334	4195	1741	33.98	2.667	1.27
J172324.87+274846.3	0490	0068	0969	0465	12.13	1.0163	0.48
J221516.18-091547.6	2262	1267	8386	3452	81.85	24.941	11.87

Both of the ratios take higher values for the case of the active galactic nuclei (AGNs). Thus, to separate out the star forming (SF) galaxies from AGNs, we make use of the BPT diagram (Baldwin et al., 1981) after correcting the emission lines, particularly the H_β line for the stellar absorption. As the emission lines used for deriving the BPT diagram are closely spaced, therefore, the corresponding integrated flux is almost independent of the internal galactic extinction and the aperture correction. Thus, the BPT diagram provides an accurate and reliable method to separate star forming galaxies from AGNs. The resultant BPT diagram computed for our

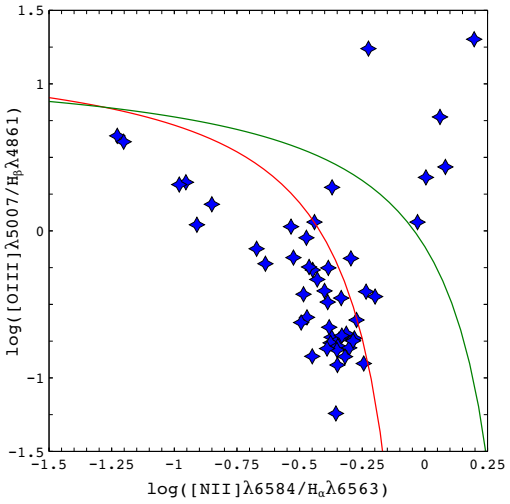

Figure 2. BPT diagram for sample galaxies. Green line is the separation between active galaxies and star forming galaxies defined by Kewley et al. (2001). Red line represent Kauffmann et al. (2003) line that separates star forming galaxies from composite ones.

sample galaxies is shown in Figure 2, which clearly separates out the AGNs from the sample. A casual look at this figure reveals that out of 50 early type emission line galaxies, 39 are of star forming type while the remaining 11 are AGNs. We used all these 39 systems for further study.

II SED fitting

The total light emanating out of a galaxy is very complex quantity and therefore the spectral energy distribution (SED) fit to the observed light offers a potential tool to disentangle the physical properties of a galaxy. Thus, the model SED provides a prediction regarding the true emission properties of a galaxy that is constructed assuming several aspects of the galaxy. However, for successful fit it not only requires information on different sources that emit photons but also requires the knowledge of the physical processes that affect the propagation of photons as they travel out of the galaxy and through the space. There are several sources that absorb, scatter and re-emit photons and hence affect greatly on the nature of the SED of their host. Further, the telescopes and the back-end instruments also put limitations on the measured values of the flux in a particular passband. As a result to fully understand the physical properties of the galaxy a proper combination of telescope and instruments is required. In addition to this, proper selection of a program to fit the modeled SED of the measured values of the galaxy flux is equally important to constrain the stellar mass, age and star formation history of the host.

A large number of codes are available for fitting SED of a galaxy light, however, majority of them suffer from limitations of the wavelength range over which they fit the measured flux values. For the present study we have made use of the publicly available spectral energy distribution (SED) fitting code MAGPHYS (Multi-wavelength Analysis of Galaxy Physical Properties) version 2 developed by (da Cunha et al., 2008) to fit the observed multi-band photometric data over the wavelength range from 912Åto 1 mm. This code used compiled libraries of model spectra of galaxies and then compares the observed flux values for a galaxy with the library

values to find the best match and is based on the Bayesian approach of fitting the UV, Optical and IR galaxy spectra and assumes an energy balance criteria so that the dust grains absorbs the intrinsic starlight energy, which is then re-emitted by it at the far-IR wavelengths. This code not only produce the realistic best-fit SEDs of a wide range of galaxies of varying characteristics but also interprets the physical properties of galaxies related with its star formation activity and dust content (Smith et al., 2012; Smith and Hayward, 2015). MAGPHYS fits the data in two steps: i. it assembles a library of model SEDs at the same redshift and in the same photometric bands as that of the detected source, and ii. determines the likelihood distribution of each of the free physical parameter of the galaxy by comparing the observed SEDs with the above created model library. The star formation histories of the program galaxies are computed by comparing the observed SEDs and the created model libraries through which it determines the likelihood distribution of the free parameters listed in Table 3.

Table 3. MAGPHYS SED fitting free parameters.

parameter	Discription
f	Fraction of L_{dust} contributed by dust in ISM
τ_v	Total effective V- band absorption depth
ψ_S	Specific star formation rate in unit per year
M_{star}	Stellar mass in $M_\odot$
$L_{dust}total$	Total luminosity absorbed by dust
T_C^{ISM}	Temperature of cold grains in thermal equilibrium in ISM
T_W^{BC}	Temperature of warm grains in thermal equilibrium in birth clouds
ξ_c^{total}	Relative ratio of cold dust in ISM
ξ_{PAH}^{BC}	Relative ratio of PAH in birth cloud
ξ_{MIR}^{BC}	Relative ratio of Mid-IR in birth cloud
ξ_W^{BC}	Relative ratio of Warm dust in birth cloud
	fraction of τ_V contributed by dust in ISM $= \tau_V^{ISM}/(\tau_V^{ISM}+\tau_V^{BC})$
M_d	Dust mass in $M_\odot$
ψ	star formation rate

MAGPHYS combines two different sets of libraries, one due to the optical starlight and the other due to the dust re-emission at IR wavelengths. The optical libraries are constructed using the (Bruzual and Charlot, 2003) simple stellar population synthesis code producing light of stars of varying metallicites in galaxies and uses the (Chabrier, 2003) initial mass function (IMF). It also compensates the data for the dust extinction of (Charlot and Fall, 2000) following that stars are formed in the dense molecular clouds, whose light is greatly attenuated by the ambient ISM.

The IR libraries are computed following (da Cunha et al., 2008) model and taking into account an assumption that the total IR luminosity of a galaxy is due to the sum of the emission from dust in the ambient ISM and that of star forming clouds (Charlot and Fall, 2000). The main components that are believed to be contributers to dust luminosity are namely, a fixed Polycyclic Aromatic Hydrocarbons (PAHs) template spectrum, mid-infrared continuum emission from hot grains heated to temperatures 130 and 250 K, emission from warm dust with

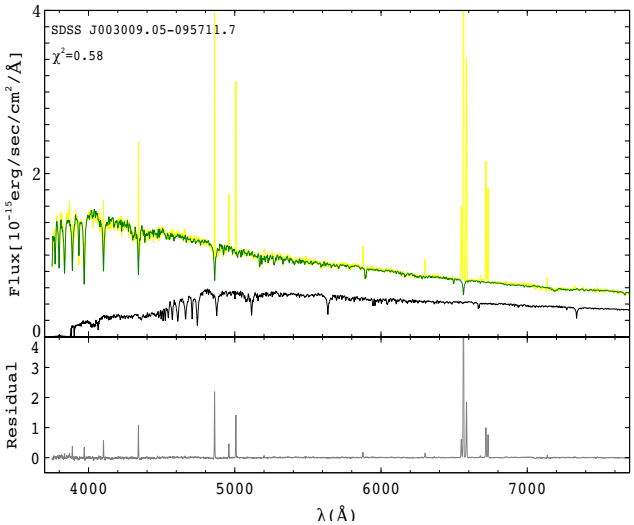

Figure 3. SPS fitting on galaxy MRK951 of our sample. *Top panel*: Observed, rest frame, dereddened spectra O_λ (yellow line) and STARLIGHT model spectra M_λ(Green line). Black line show Galaxy spectra after removal of 0.1 Gyr younger population obtained by REMOVEYOUNG code.*Bottom panel*:Residual spectrum $(O_\lambda - M_\lambda)$

adjustable temperature of 30-60K and that from the cold grains with temperature in the range of 15-25 K (da Cunha et al., 2010).

For fitting SED to the measured flux values from starburst and star forming galaxies, we need to remove the extra contribution due to the nebular emission lines in the optical (ugr) photometric bands. This nebular emission contribution from the stellar light was removed by employing the code *REMOVEYOUNG* developed by (Gomes and Papaderos, 2016), which takes care of removing the contribution from stellar population younger than the adjustable age cutoff from the observed galaxy population. For this purpose it uses the population vector information generated by the spectral population synthesis (SPS) model as an input. Population vector represents the mass fraction of the best stellar population mixture obtained by SPS model that depends on the age, metallicity and initial mass function (IMF) of stellar population. We further use the *STARLIGHT* SPS model (Cid Fernandes et al., 2005) that combines a linear combination of 45 simple stellar populations from evolutionary synthesis model (Bruzual and Charlot, 2003) with metallicity values $Z = 0.2, 1, 2.5Z_\odot$ for stellar ages 0.001, 0.00316, 0.005, 0.01, 0.025, 0.04, 0.102, 0.286, 0.640, 0.905, 1.434, 2.5, 5, 11 and 13 Gyr considering Chabrier (2003) IMF to fit the observed redshift corrected, galactic extinction corrected re-binned spectrum. Here we adopt Calzetti (1997) extinction law with $R_V = 3.1$ for extinction correction. We masked strong emission lines during the fit. The population vectors obtained in this way contain information about the star formation history of galaxy and include imformation such as stellar mass, extinction, velocity dispersion, mean stellar ages and mean stellar metalicities.Poupulation vector obtained so were then used as input to *REMOVEYOUNG* code with the cut off age of 0.1 Gyr and hence obtain the contribution of nebular emission lines to optical photometric bands, which was then removed from the respective filter flux value. The best fitted results of the *STARLIGHT* and the *REMOVEYOUNG* fit after removing contribution from stellar population younger than 0.1Gyr is shown in Figure 3. Residual plot represent $(O_\lambda - M_\lambda)$. After removing this contribution of nebular emission lines in the optical photometric (*ugr*) filters we fitted the resultant flux values with the SED using MAGPHYS. The best fit SED representative for SDSS

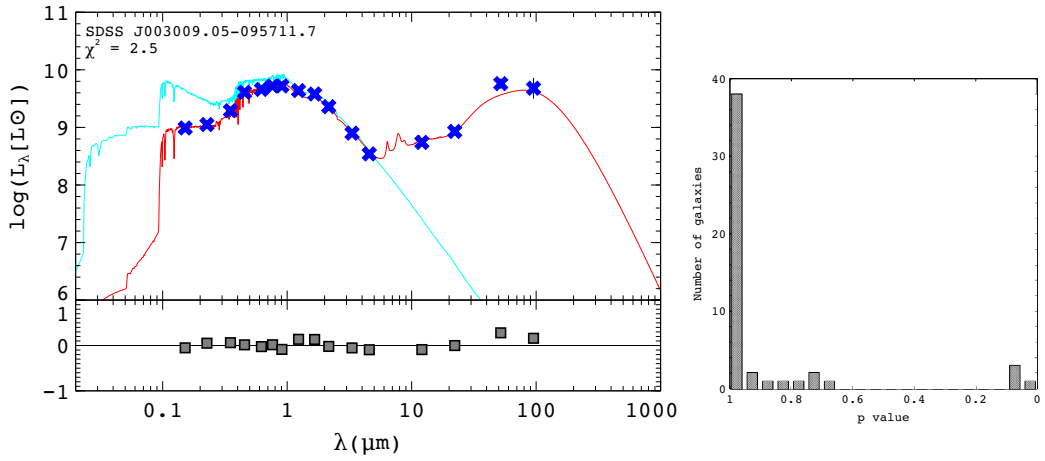

Figure 4. *Left panel*-SED fitting on photometric data of first galaxy of our sample MRK951.Attenuated and unattenuated spectra are shown in red and cyan color respectively.Blue cross points show photometric data points used for fitting.Bottom panel represent the fit residual $[(L_\lambda^{obs} - L_\lambda^{model})/L_\lambda^{obs}]$.*Right panel-p*-value for MAGPHYS fit for all sample galaxies.

J003009.05-095711.7 is shown in Figure 4. We repeated this exercise of fitting SEDs to the resultant flux values of all the galaxies from our sample. The best fit SED yielded several physical parameters of the sample galaxies, which includes SFR ($\psi_{MAGPHYS}$), stellar mass(M_{star}) and dust mass(M_{dust}), specific star formation rate(ψ_s) and are listed in Table 3 . We found that SEDs for majority of the galaxies from our sample are well constrained. In few cases the SED fits were not constrained well. The quality of the fit was checked from the χ^2 values, which is an indicator of the goodness of the model fit compared to the data points. As the χ^2 value is highly sensitive to the quality of the data and the number of data points, therefore, there is not a general limit for its value that can be considered as an unreliable fit. However, the quality of the fit can be judged only on the basis of comparing the fitted SED with that of the observed one. Further, the *Degrees of freedom (dof)* is not equal to the number of photometric data points used to fit the SED as each of the data point is affected by the neighboring data points. Therefore, we calculated the *dof* for each of the system following the procedure outlined in Smith et al. (2012). We tried to express the quality of the SED fit to the data points on each of the galaxy by deriving the *p*-value, which depends on the measured χ^2 values and the *dof* (Clauset et al., 2009). Here, the p-value for the goodness-of-fit evaluation is defined as the probability the chi-square test statistics could take higher value if the null hypothesis were true.It represent the significance value of the fit and depends on measured χ^2 values and the *dof*. Histogram of the resultant *p*-value of the best fit SEDs for significance level 0.05 is shown in right panel of Figure 4, which shows a peak near 1 confirming that the quality of the SED fit was appreciable. Also, we have calculated stellar masses of sample galaxies from SDSS photometric data (Taylor et al., 2011) and are compared with stellar masses of galaxies estimated using MAGPHYS as shown in left panel of Figure 5. Code STARLIGHT also gives Stellar mass of galaxies but is only associated with the galaxy stellar mass covered by SDSS fiber.

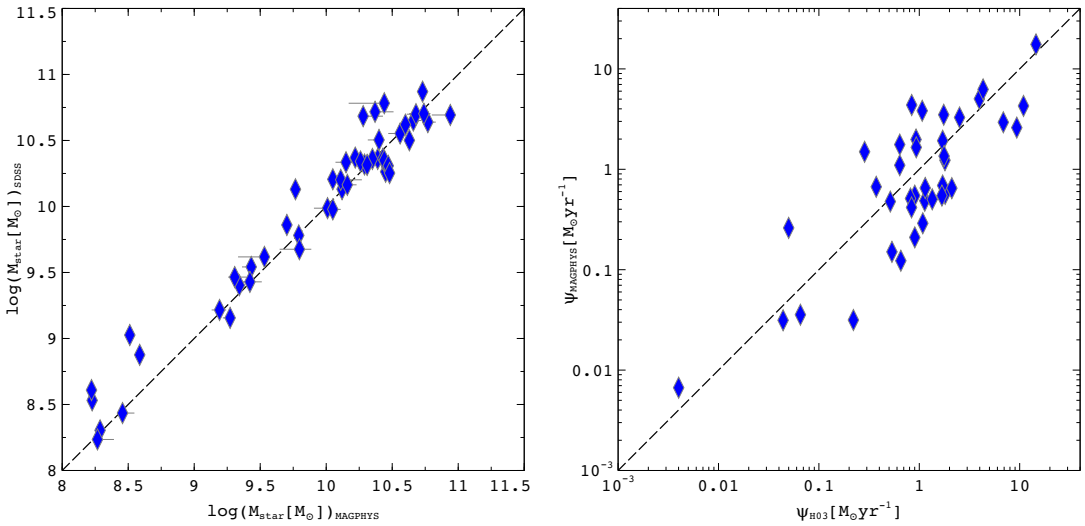

Figure 5. *Left panel*-Stellar mass obtained by MGAPHYS SED fitting Vs Stellar masses obtained using SDSS data (Taylor et al., 2011).Dotted line show 1:1 relation. *Right panel*-SFR determined by spectroscpy using Hopkins et al. (2003) relation(*eq 10*)Vs SFR estimated by MAGPHYS SED fitting. Solid line show 1:1 relation.

III Color-Magnitude diagram

Multi-wavelength photometric data on galaxies are the key to understand the physical processes that are operative within the galaxies. Due to its vast spectroscopic and accurate multi-band photometric surveys in the local universe the SDSS surveys have played a significant role in robust statistical analysis of galaxy populations. Particularly, the *color - magnitude* or *color - mass* diagram (CMD) (e.g., $u-r$ vs. r band absolute magnitude) constructed with the SDSS photometric observations for the field galaxies have exhibited two different peaks, one narrower red peak and the other wider blue peak, in their optical color distribution (Strateva et al., 2001; Baldry et al., 2004). The former was like that seen for the cluster galaxies and was referred to as the *red sequence*, while the later were referred to as the *blue cloud* (Kauffmann et al., 2003). Interestingly, it was noticed that the galaxies belonging to the red sequence on average hosts older stellar population, higher surface stellar mass densities with the total stellar content larger than $10^{10.5} M_{\odot}$ (Salim et al., 2015) while those in the blue cloud exhibit current star formation. This *bimodality* in color distribution of the galaxies acted as an important tool not only for the studies of local galaxies but also for those at higher redshifts. Faber et al. (2007) observed that the luminosity-function for the red-sequence galaxies increases by a factor of two or even large at the redshift of $z \sim 1$. This increase in the luminosity function imply that the build-up of the red-sequence galaxies is an ongoing process until the present epoch. This observation is against the traditional picture of the ETGs, where we believe that the stars in ETGs have formed in early epochs through the monolithic collapse and have stopped star formation at later epochs making them to appear redder. However, the optical bimodality identifies the star-forming ETGs even in the present epoch, probably pointing towards the late-epoch formations of the ETGs through the merger like processes and hence possibly explain the observed growth of the red-sequence members. If this model of ETG formation is valid then we can expect a group of galaxies in the transition phase, whose properties lie in between the red-sequence and the blue-cloud mem-

Table 3. MAGPHYS output parameter values.

SDSS Id	χ^2	$log(\psi[M_\odot])$	$log(M_{star}[M_\odot])$	$log(\psi_s[yr^{-1}])$	$log(M_{dust}[M_\odot])$
SDSS J003009.05-095711.7	2.51	-0.313^{0}_{0}	9.79^{0}_{0}	-10.12^{0}_{0}	6.41^{0}_{0}
SDSS J003823.71+150222.4	1.52	$-0.911^{0.05}_{0.78}$	$10.39^{0.06}_{0.08}$	$-10.47^{0.9}_{0}$	$7.81^{0.67}_{0.14}$
SDSS J010358.74+151450.1	0.49	$0.041^{0.06}_{0.16}$	$10.66^{0.06}_{0.05}$	$-10.62^{0.1}_{0.2}$	$7.73^{0.49}_{0.40}$
SDSS J012729.23-083315.4	3.08	$0.631^{0}_{0.01}$	$10.73^{0}_{0.01}$	-10.12^{0}_{0}	$8.13^{0.31}_{0.16}$
SDSS J022628.28+010937.7	5.70	-1.501^{0}_{0}	$8.59^{0}_{0}0$	-10.07^{0}_{0}	$5.10^{0.49}_{0.3}$
SDSS J023247.42+004041.1	2.13	0.583^{0}_{0}	8.51^{0}_{0}	-7.93^{0}_{0}	$7.43^{0}_{0.34}$
SDSS J030349.10-010613.4	12.71	$0.307^{0}_{0.12}$	$10.94^{0}_{0.14}$	$-10.62^{0.05}_{0}$	$8.65^{0.32}_{0.52}$
SDSS J075912.37+533325.9	0.91	0.702^{0}_{0}	10.45^{0}_{0}	-9.78^{0}_{0}	$7.35^{0.53}_{0.37}$
SDSS J080740.99+390015.2	7.20	-0.018^{0}_{0}	10.22^{0}_{0}	-10.22^{0}_{0}	$6.82^{0.08}_{0}$
SDSS J081616.93+255827.9	2.35	0.167^{0}_{0}	$10.05^{0}_{0.01}$	-9.88^{0}_{0}	$6.71^{0.37}_{0.13}$
SDSS J082938.74+520434.8	5.75	-0.584^{0}_{0}	8.23^{0}_{0}	-8.83^{0}_{0}	$5.68^{0.09}_{0}$
SDSS J085139.06+570626.6	0.37	$-0.678^{0.14}_{0.08}$	$10.01^{0.01}_{0.10}$	$-10.57^{0.1}_{0.05}$	$6.12^{0.47}_{0.45}$
SDSS J085311.41+370806.5	1.06	$0.5166^{0.05}_{0.04}$	$10.68^{0.1}_{0.07}$	$-10.12^{0.1}_{0.15}$	$7.23^{0.25}_{0.16}$
SDSS J094150.95+121101.5	2.25	-0.186^{0}_{0}	9.70^{0}_{0}	-9.88^{0}_{0}	$6.45^{0.28}_{0.02}$
SDSS J094403.20+293634.0	1.98	$-0.683^{0.21}_{0.05}$	$10.05^{0.06}_{0.07}$	$-10.72^{0.3}_{0.05}$	$6.22^{0.36}_{0.28}$
SDSS J094941.20+321315.9	1.19	$-1.323^{0}_{0.04}$	$9.27^{0}_{0.05}$	-10.57^{0}_{0}	$5.50^{0.42}_{0.42}$
SDSS J095700.62+595808.0	3.19	$0.285^{0.03}_{0.02}$	$10.29^{0.02}_{0.07}$	$-10.02^{0.09}_{0}$	$7.32^{0.21}_{0.21}$
SDSS J100351.88+592610.3	2.56	$-0.299^{0.02}_{0}$	$9.43^{0}_{0.07}$	$-9.73^{0.1}_{0}$	6.17^{0}_{0}
SDSS J100604.28+534253.4	1.16	$0.397^{0.12}_{0.28}$	$10.15^{0.18}_{0.08}$	$-9.83^{0.2}_{0.19}$	$7.57^{0.51}_{0.33}$
SDSS J101720.02+152920.9	3.57	$0.796^{0.01}_{0.13}$	9.77^{0}_{0}	$-8.98^{0}_{0.15}$	$8.43^{0.39}_{0.74}$
SDSS J101912.56+635802.6	4.07	1.272^{0}_{0}	$10.28^{0.15}_{0}$	$-9.03^{0}_{0.1}$	$8.37^{0.06}_{0.02}$
SDSS J102158.91+645847.9	1.32	$0.090^{0.09}_{0.03}$	$10.35^{0}_{0.01}$	-10.22^{0}_{0}	$7.03^{0.48}_{0.39}$
SDSS J103106.76+284747.9	2.41	-0.822^{0}_{0}	$9.42^{0.09}_{0.12}$	$-10.27^{0.25}_{0.2}$	$6.12^{0.06}_{0.02}$
SDSS J104549.80+273711.2	2.36	1.244^{0}_{0}	$10.37^{0.14}_{0}$	$-9.13^{0}_{0.1}$	$7.87^{0.02}_{0}$
SDSS J105437.89+553945.7	0.41	$-0.244^{0.21}_{0.18}$	$10.26^{0}_{0.14}$	$-10.42^{0.1}_{0}$	$6.62^{0.58}_{0.61}$
SDSS J111349.74+093510.7	1.24	$0.562^{0}_{1.45}$	$10.44^{0}_{0.27}$	$-9.88^{0}_{1.2}$	$7.91^{0.09}_{1.36}$
SDSS J111632.33+284635.3	0.99	$0.640^{0}_{0.03}$	$9.53^{0}_{0.2}$	$-11.87^{0.15}_{0}$	$6.58^{0.49}_{0.42}$
SDSS J111732.39+512553.8	16.26	$0.175^{0}_{1.45}$	$8.46^{0.09}_{0}$	$-8.28^{0}_{0.1}$	$6.88^{0.69}_{1.36}$
SDSS J114556.60+501159.0	3.73	$-1.504^{0.01}_{0}$	8.29^{0}_{0}	-9.78^{0}_{0}	$5.78^{0.43}_{0.16}$
SDSS J114700.72-001739.2	13.78	$-1.449^{0}_{0.03}$	$8.22^{0.01}_{0}$	-9.68^{0}_{0}	$5.06^{0.92}_{0.12}$
SDSS J115147.62+484059.2	2.02	$-0.878^{0.10}_{0.02}$	$9.19^{0.05}_{0.06}$	$-10.07^{0}_{0.15}$	$6.53^{0.48}_{0.44}$
SDSS J120617.05+633819.0	2.39	0.468^{0}_{0}	$10.40^{0}_{0.08}$	$-9.93^{0.15}_{0}$	$7.50^{0.42}_{0.19}$
SDSS J120823.52+000636.9	1.51	$-0.174^{0.10}_{0.02}$	$10.56^{0.01}_{0.09}$	$-10.77^{0}_{0.1}$	$7.01^{0.48}_{0.44}$
SDSS J121035.68+114538.9	5.01	$-2.176^{0.08}_{0}$	$8.27^{0}_{0.12}$	$-10.52^{0.34}_{0}$	$5.19^{0.41}_{0.37}$
SDSS J123502.64+662233.4	1.89	$0.296^{0.06}_{0.09}$	$10.77^{0.06}_{0.01}$	$-10.47^{0.15}_{0.05}$	$7.37^{0.51}_{0.39}$
SDSS J124813.65-031958.2	3.58	$-0.262^{0.41}_{0}$	$9.80^{0.09}_{0.15}$	$-10.07^{0.24}_{0.1}$	$6.35^{0.30}_{0.14}$
SDSS J125651.17+265355.9	0.94	-0.44^{0}_{0}	10.12^{0}_{0}	-10.57^{0}_{0}	$6.74^{0.44}_{0.37}$
SDSS J125725.24+272416.4	0.18	$-0.763^{0}_{0.01}$	$9.34^{0}_{0.01}$	-10.12^{0}_{0}	$5.88^{0.32}_{0.22}$
SDSS J125835.33+271552.8	11.06	-0.161^{0}_{0}	$9.31^{0.09}_{0.05}$	$-9.48^{0.05}_{0.14}$	$6.83^{0.44}_{0.37}$
SDSS J134747.70+111626.9	0.80	$0.246^{0}_{0.01}$	$10.43^{0.01}_{0.15}$	$-10.17^{0}_{0.24}$	$7.33^{0.32}_{0.22}$
SDSS J140747.19+523809.7	0.79	$0.219^{0.06}_{0.08}$	$10.11^{0}_{0.16}$	$-9.88^{0}_{0.2}$	$7.08^{0.32}_{0.2}$
SDSS J141433.22+404522.9	2.38	$0.543^{0}_{0.4}$	$10.46^{0}_{0.02}$	$-9.93^{0.15}_{0}$	$7.47^{0.26}_{0.51}$
SDSS J143222.70+565108.3	1.83	$0.132^{0}_{0.04}$	$10.74^{0.05}_{0.11}$	$-10.62^{0.05}_{0.15}$	$7.07^{0.15}_{0.19}$
SDSS J151809.64+254211.5	2.64	$-0.188^{0.1}_{0.01}$	$10.44^{0.01}_{0}$	-10.62^{0}_{0}	$7.15^{0.3}_{0.02}$
SDSS J155000.46+415811.1	1.77	$-0.291^{0.06}_{0.05}$	$10.47^{0}_{0.01}$	-10.67^{0}_{0}	$6.82^{0.2}_{0.17}$
SDSS J155335.56+321820.5	2.07	$-0.380^{0.02}_{0}$	$10.31^{0.02}_{0.01}$	$-10.67^{0}_{0.1}$	$6.37^{0.5}_{0.32}$
SDSS J160753.98+200303.7	2.49	-0.262^{0}_{0}	$10.16^{0}_{0.06}$	$-10.42^{0}_{0.05}$	$6.72^{0.12}_{0.09}$
SDSS J164430.75+195626.7	1.81	$-0.538^{0}_{0.18}$	$10.48^{0}_{0.01}$	-11.02^{0}_{0}	$7.51^{0.31}_{0.41}$
SDSS J172324.87+274846.3	2.22	$-0.321^{0.08}_{0.02}$	10.63^{0}_{0}	-10.92^{0}_{0}	$6.64^{0.33}_{0.24}$
SDSS J221516.18-091547.6	0.76	0.415^{0}_{0}	10.60^{0}_{0}	-10.17^{0}_{0}	$7.74^{0.57}_{0.20}$

bers. Salim (2014) could identify the systems in transition class as the *green valley* objects.The green-valley represent the class of galaxies having mixed population of stars and contain lowest massive black holes at their centers that are ignited through a steady supply of mass from blue cloud progenitor (Schawinski et al., 2010). Green-valley galaxies represent the sites where

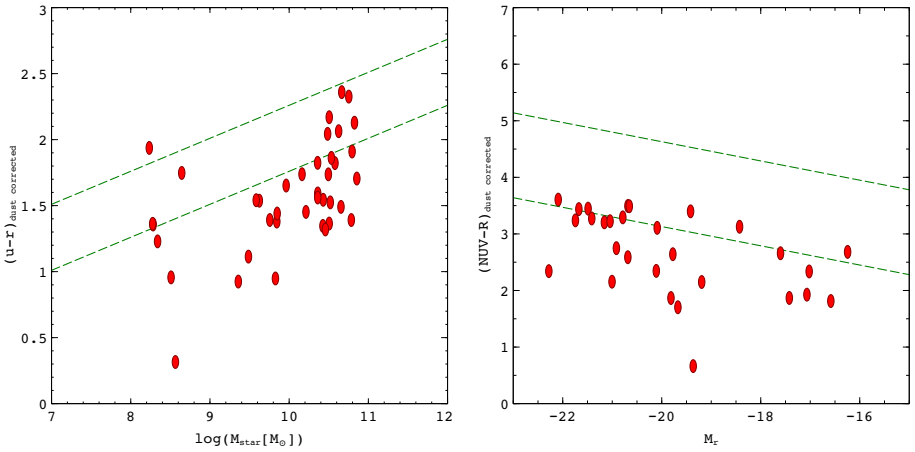

Figure 6. *left panel*-Color (u-r) vs Stellar mass(converted to Kroupa (2001) IMF) of SF sample galaxies.color (u-r) is galactic extinction corrected, intrinsic dust corrected and k corrected.Region within two solid lines represent *Green Valley* region (Schawinski et al., 2014)*right panel*-Color(NUV-R) vs Absolute R band magnitude for SF sample galaxies.Region within two solid lines represent *Green Valley* region (Guo et al., 2016).

star formation shuts down and The *duty cycle* of the AGN hosted by the present day early-type galaxy population is maximally observed. Thus, the use of the CMD for this class of galaxies confirm the fact that the photometric multi-band data on these systems is useful to trace their evolutionary stages. As a result, we have made use of the multi-band photomteric data on the sample galaxies to plot the $(u - r)$ color against their stellar mass content and the resultant graph is shown in left panel of Figure 6. The measured values of colours were corrected for the internal dust extinction using H_α and H_β line flux ratios derived above. Here, the color excess $E(B - V)$ for stellar continuum were estimated using relation given by Calzetti (2001) and the attenuation law of Calzetti (1997). This *color-mass* plot clearly reveal that majority of the galaxies from our sample fall in the class of star forming galaxies.

Another promising way of delineating the SF activity in the ETGs was to use the *ultraviolet* (UV) photometric observations of the galaxies. As UV bands cover the peak of the black-body emission originating from young and hot stars relative to the optical passbands that cover emission dominated by older population, therefore, reflect the current star formation (Kennicutt, 1998). The space telescope *Galaxy Evolution Explorer* (GALEX) has observed several thousand square degrees of the sky in two UV passbands namely, far-UR (FUV) and near-UV (NUV). These observations largely overlap with the SDSS data and, therefore, if both these observations are coupled together provide a more suitable way of investigating the SF in this class of galaxies. In fact, the combined data sets from the *GALEX* and *SDSS* has led to the discovery of the *green valley* objects, that are in between the active SF and the passive red-sequence galaxies with star formation rates lower than the actively SF class of galaxies (Salim, 2014). The *green valley* becomes even more important when the rest-frame NUV magnitude is coupled with that of the r-band magnitude. Owing to this advantage we have also made an attempt to plot the CMD between the $NUV - r$ colour versus absolute r band magnitude (M_r) of the star forming galaxies from our sample and the resultant plot is shown in right panel of Figure 6. Before that the NUV magnitudes have been corrected for the internal galactic dust extinction following (Cardelli et al., 1989). A casual inspection of the $NUV - r$ colour versus M_r *color-magnitude* plot for our sample revealed that majority of them fall either in the *green*

valley or the *blue cloud* class, implying that they are star formation galaxies.

IV Star formation rates

There are a number of monochromatic as well as hybrid star formation rate (SFR) estimators of galaxies employing measured values of emission flux values over the wide range of electromagnetic spectrum. In the present case we have used the traditional H_α emission line flux values as a SFR estimator. After modifying the Kennicutt (1998) relation employing the Chabrier (2003) IMF, the revised expression of SFR (ψ_{K98} hereafter) becomes

$$SFR = \frac{L(H_\alpha)}{2.1 \times 10^{41}} M_\odot/yr \tag{9}$$

where, $L(H_\alpha)$ represents the internal extinction and aperture corrected H_α nebular line luminosity. Independently, we have also estimated the luminosity of the H emission line for the sample of SF galaxies and corresponding star formation rates (ψ_{H03} hereafter)using equivalent widths of the H emission lines and employing the relation given by Hopkins et al. (2003) as

$$L_{H_\alpha,int} = (EW_{H\alpha} + EW_c) \times 10^{-0.4(M_r - 34.10)} \times \frac{3 \times 10^{18}}{[6564.61(1+z)]^2} \times \left(\frac{F_{H\alpha}}{F_{H\beta}}\right)^{2.36} \text{ergs}^{-1} \tag{10}$$

where, M_r is galactic extinction corrected, k corrected absolute r band magnitude, F_{H_α} and F_{H_β} are the aperture, intrinsic dust absorption and stellar absorption corrected H_α and H_β emission line flux values, respectively. We consider a constant stellar absorption correction factor EW_c = 2.6 Åfor the H_α emission line for the case of SF galaxies. Star formation rates estimated by direct measurement of H_α luminosity through *deblending task* and measurement of H_α luminosity using H_α equivalent widths are in good agreement with one another and are as shown in left panel of Figure 7.Star formation rates derived spectroscopically and that obtained by MAGPHYS SEDs are also in very good agreement with each other and as shown in right panel of Figure 4.

It is established that the interstellar dust plays an important role in the star formation in host galaxies acting as a catalyst (Patil et al., 2007). As total dust content of a galaxy is a reliable output of the SED fitting, therefore, we also quantify the SFR in the program galaxies employing MAGPHYS delivered dust masses.The variation of galaxy dust mass M_{dust} with Star formation rate $\psi_{MAGPHYS}$ for sample galaxies is as shown in right panel of Figure 7.The solid line represent the best fit with expression

$$log(\psi[M_\odot yr^{-1}]) = (7.0149 \pm 0.070) + (0.9807 \pm 0.098) \times log(M_{dust}[$$

$M_\odot$])] $which is in good agreement with the relation given by da Cunha et al.$ (2010).

Gas(in atomic or molecular form) present in galaxy plays a vital role in star formation as well as black hole growth since both these phenomena start growing by gas fuel present in the host galaxy.Thus the fate of the galaxy will be decided by the abundance of the gas present in host galaxy. With an objective to examine the dependence of the SF activity in the host with its gas content we have made use of the estimates of dust mass for calculating total gas content (both atomic as well as molecular gas) of the galaxies using the M_{Dust} -M_{gas} relation proposed by Corbelli et al. (2012). Here, the gas fraction f_{gas} is defined as f_{gas}=$M_{gas}/(M_{gas}$ +

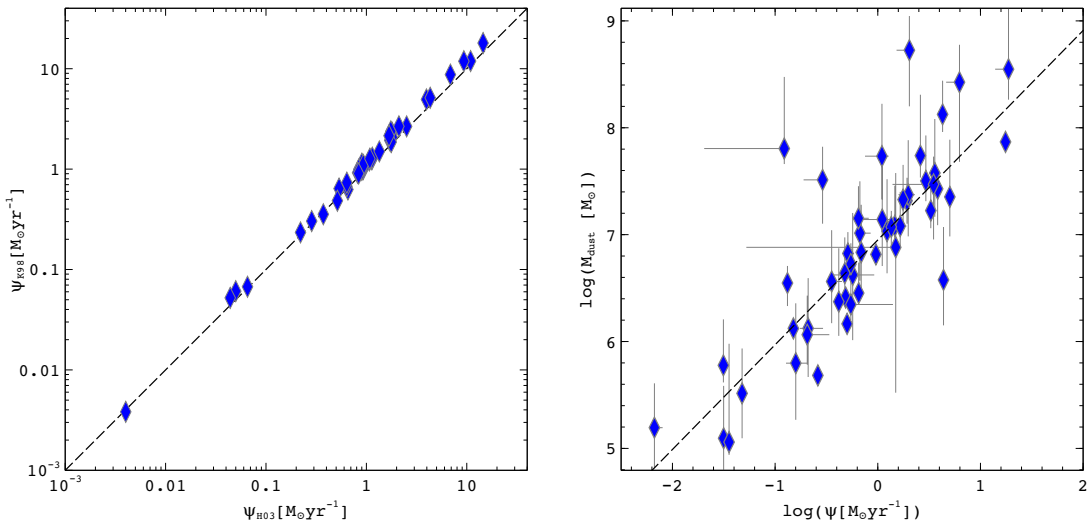

Figure 7. *left panel*-variation of SFR determined using $H\alpha$ equivalent width(*eq(10)*)with SFR calculated using direct measurement of $H\alpha$ flux through debelnding in SPLOT(*eq(09)*). Solid line show 1:1 relation *Right panel-*

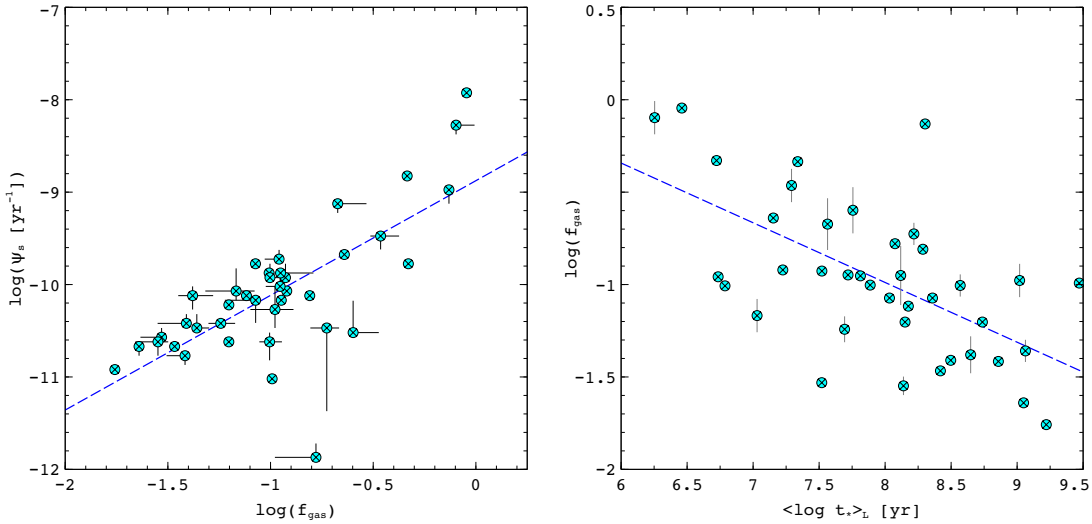

Figure 8. *left panel*-Variation of specific SFR with gas fraction. Dotted line show the best fit line represented by equation; $log(\psi_s) = (1.241 \pm 0.1993) \times log(f_{gas}) - (8.876 \pm 0.2106)$ with correlation coefficient 0.71.*Right panel*-fraction of the gas present in galaxy as a function of light weighted average stellar age of galaxy population.

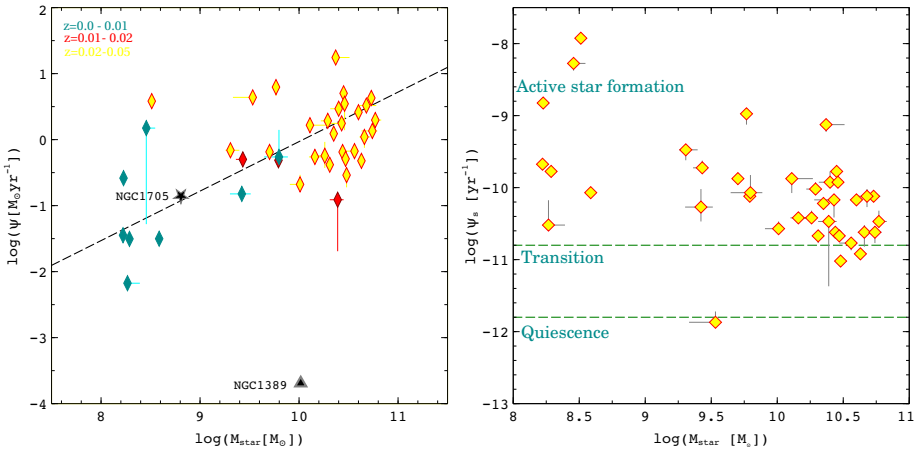

Figure 9. Stellar mass vs SFR for Star forming galaxies.Solid line represent *main Sequence* relation defined by (Renzini and Peng, 2015).A starburst elliptical NGC1705 and a normal red and dead elliptical NGC1389 are also plotted for reference (Vaddi et al., 2016).*Right panel*-Dependence of specific star formation rate on stellar mass of galaxy.dotted lines confine *Green valley* region(Salim, 2014)

M_{star}).Sample SF galaxies show average fraction of gas over a total baryonic mass of host galaxy $f_{gas} = 17.68\%(with f_{gas[min]} = 1.74\% and f_{gas[max]} = 90.11\%)$,showing the availability of little gas to sustain further star formation in the galaxy.We tried to find dependence of specific star formation rate (ψ_s) on the estimated gas fraction (F_{gas}). The resultant correlation is shown in left panel of Figure 7. This plot reveals that SFR is more in gas rich systems and yields a best fit equation $log(sSFR) = (1.24 \pm 0.19) \times log(f_{gas}) - (8.87 \pm 0.21)$ with the correlation coefficient of 0.71. In order to study the gas content of galaxy over the average stellar age, we have determined the average light weighted stellar age using the population vector for sample galaxies obtained using equation $< log(t) >_L = \sum x_j log(t_j)$ where j is ranging from 1 to 45.The gas fraction of galaxy is found to be decreasing with increasing stellar age, the result is supporting the findings of (Kokusho et al., 2017).The result confirm a very strong dependence of specific star formation rate on the gas content of galaxy over the average stellar age of galaxy population and implies that the star formation in these ETG is purely of intrinsic origin.

V Correlation between the Stellar mass content and the SFR

Several of the physical properties of a galaxy including, star formation history, AGN activity, etc. are greatly influenced by the stellar mass content of the host. Recent studies have confirmed a strong correlation between the star formation rate (SFR) of galaxies versus their stellar mass content (M_{star}), exhibiting the *main-sequence* (MS) of the star-forming galaxies (Brinchmann et al., 2004; Salim et al., 2007). This MS plane provides a powerful tool to investigate the evolutionary stages of the star forming galaxies. As a result we have also made an attempt to investigate the correlation between the stellar content of the program galaxies (M_{star}) versus their SFRs derived above and the resultant correlation is shown in the left panel of Figure 9. As all the galaxies from our sample are nearby with redshifts less than 0.05, therefore, the mass-incompleteness is not an issue (Bait et al., 2017). For comparison we also highlight the positions of a starburst galaxy NGC 1705 and a normal read and dead elliptical galaxy NGC 1389 in this figure, data points retrieved from (Vaddi et al., 2016). A casual inspection of this

plot reveals that majority of the galaxies from our sample follow the *main sequence* plane, known as the *Star-Forming* pattern of Renzini and Peng (2015). This in turn confirms that nearly all the systems from our sample are undergoing a continuous star formation. A couple of systems from our sample are found to occupy positions above the *main sequence* suggesting that they are passing through the starburst phase, while those which are lying below the *main sequence* belong to the group of the *green valley* region (Wyder et al., 2007). The *green valley* systems are believed to represent the transition zone between the actively star forming galaxies (the *blue cloud* and the passively evolving *red-sequence* quiescent galaxies (Wyder et al., 2007; Schiminovich et al., 2007) and hence exhibit a two way flow of the galaxy evolution. This means, the star formation in the *green valley* systems is either triggered one (making them to move from the red-sequence to the blue-cloud) or quenched one (moving from blue-cloud to the red-sequence) due to some internal or external influence like, merging of galaxies or AGN outburst, respectively (Pandge et al., 2012; Sonkamble et al., 2015). A relatively clear picture for the evolutionary track of galaxies was provided by the improved version of the correlation between the specific star formation rate (sSFR) i.e., the rate of young star formation versus the existing stellar mass (M_{star}) and is shown in the right panel of Figure 9. The dotted green line labeled as the transition zone in this plot represents the green valley systems (Salim, 2014). From this plot it is clear that nearly all the 39 systems from our present sample that were identified as the star forming galaxies in the BPT diagram (Figure 5) turns out to be systems with the intense star formation activity.

IV Conclusion

This paper presents a spectro-photometric study of a sample of 50 early-type galaxies from within local universe with redshift in the range between $0 < z < 0.05$ with an objective to investigate their star formation processes. We have performed SED fitting over UV to far-IR spectro-photometric data on each of the galaxy from our sample by employing MAGPHYS code. This fitting yielded several physical properties including dust content, stellar content of the galaxy, star formation rate, etc. Main results from this study are summarized below:

- We fit SED to the measured values flux densities over the wavelength range from between UV to far-IR acquired using various instruments after applying various corrections including stellar population synthesis using code MAGPHYS. SEDs fits to the observed data were well constrained for majority of the galaxies from present sample. This fitting yielded several physical parameters for each of the program galaxy including, the dust mass, stellar content, star formation rate, quality of fit, etc.

- SED fit revealed that nearly all the systems from our sample exhibit star formation, however, it is believed that the SFR in a galaxy is also influenced by the nuclear activity at the core of the host. Therefore, it was required to isolate such systems with AGN activity. This was done computing the BPT diagram based on the strengths of the optical line flux ratios. The BPT diagram for the present sample enabled us to isolate 11 galaxies as AGNs, while 39 remaining as the star forming galaxies.

- The colour-magnitude diagram derived after employing attenuation correction for the sample galaxies revealed a bimodality like that seen in the optically selected galaxies. A

transition class, the *green valley*, exhibiting characteristics in between the red-sequence and blue-cloud galaxies has also been observed in the CMD implying that these galaxies show star-formation activity. Though most of the galaxies are of red sequence type, but few were found to occupy position in the blue cloud region.

- The galaxies in *green valley* show a good fractions of SFRs with members younger than expected normal ETGs. Thus, the sample of ETGs in present study therefore represent a different formation scenario, like that formed through the interaction or merger like events and therefore are far from being red and dead systems.
- We use different independent SFR estimators: SED-based, dust mass based, measured H_α emission line flux densities and that estimated using the equivalent widths of the H_α Balmer line, and find the closest agreements among all the SFR estimates.
- Strong correlations have been evidenced in the SFR and the dust as well as the stellar content of a galaxy. A similar correlations has been evidenced in the specific star formation and the gas fraction of a galaxy.
- Nearly all the SF galaxies from our sample are low mass galaxies with the average mass less than $8.1\times\ 10^9\ M_\odot$ and hence support the investigation by Kanappan et al. that star formation is seen normally in low mass galaxies irrespective of their morphological classification.
- The detailed analysis of specific star formation rates, dust corrected UV-r colours and other properties of the star forming galaxies revealed evolution of the ETGs through the green valley.
- As far as origin of the SF in these galaxies is concerned, it is likely that SF activity in ETGs in local universe is mainly triggered by the minor mergers of gas-rich systems, in turn suggest the external origin of the gas for SF.

ACKNOWLEDGEMENTS

The SDSS is managed by the Astrophysical Research Consortium for the Participating Institutions. The Participating Institutions are the American Museum of Natural History, Astrophysical Institute Potsdam, University of Basel, University of Cambridge, Case Western Reserve University, University of Chicago, Drexel University, Fermilab, the Institute for Advanced Study, the Japan Participation Group, the Johns Hopkins University, the Joint Institute for Nuclear Astrophysics, the Kavli Institute for Particle Astrophysics and Cosmology, the Korean Scientist Group, the Chinese Academy of Sciences (LAMOST), Los Alamos National Laboratory, the Max Planck Institute for Astronomy (MPIA), the Max Planck Institute for Astrophysics (MPA), New Mexico State University, Ohio State University, University of Pittsburgh, University of Portsmouth, Princeton University, the United States Naval Observatory, and the University of Washington. This work also uses data acquired with the NASA Galaxy Evolution Explorer. GALEX is operated for NASA by the California Institute of Technology under NASA contract NAS5-98034.This publication makes use of data products from the Two Micron All Sky Survey (2MASS), which is a joint project of the University of Massachusetts and the Infrared Processing and Analysis Center/California Institute of Technology, Star-Formation Bimodality in Early-Type Galaxies 15 funded by the National Aeronautics and Space Administration and the National Science Foundation. This publication makes use of data products from the Wide-field Infrared Survey Explorer, a joint project of the University of California, Los Angeles, and the Jet Propulsion Laboratory/California Institute of Technology, funded by the National Aeronautics and Space Administration. Some of the data presented in this paper were obtained from the Mikulski Archive for Space Telescopes (MAST). STScI is operated by the Association of Universities for Research in Astronomy, Inc., under NASA contract NAS5-26555. This research has made use of the NASA/IPAC Extragalactic Database (NED) which is operated by the Jet Propulsion Laboratory, California Institute of Technology, under contract with the National Aeronautics and Space Administration.

References

Abazajian, K. N., Adelman-McCarthy, J. K., Agüeros, M. A., Allam, S. S., Allende Prieto, C., An, D., Anderson, K. S. J., Anderson, S. F., Annis, J., Bahcall, N. A., and et al. (2009). The Seventh Data Release of the Sloan Digital Sky Survey. , 182:543–558.

Bait, O., Barway, S., and Wadadekar, Y. (2017). On the interdependence of galaxy morphology, star formation, and environment in massive galaxies in the nearby Universe. *ArXiv e-prints*.

Baldry, I. K., Glazebrook, K., Brinkmann, J., Ivezić, Ž., Lupton, R. H., Nichol, R. C., and Szalay, A. S. (2004). Quantifying the Bimodal Color-Magnitude Distribution of Galaxies. , 600:681–694.

Baldwin, J. A., Phillips, M. M., and Terlevich, R. (1981). Classification parameters for the emission-line spectra of extragalactic objects. , 93:5–19.

Barton, E. J., Geller, M. J., and Kenyon, S. J. (2000). Tidally Triggered Star Formation in Close Pairs of Galaxies. , 530:660–679.

Bell, E. F., Wolf, C., Meisenheimer, K., Rix, H.-W., Borch, A., Dye, S., Kleinheinrich, M., Wisotzki, L., and McIntosh, D. H. (2004). Nearly 5000 Distant Early-Type Galaxies in COMBO-17: A Red Sequence and Its Evolution since z˜1. , 608:752–767.

Brinchmann, J., Charlot, S., White, S. D. M., Tremonti, C., Kauffmann, G., Heckman, T., and Brinkmann, J. (2004). The physical properties of star-forming galaxies in the low-redshift Universe. , 351:1151–1179.

Brown, M. J. I., Dey, A., Jannuzi, B. T., Brand, K., Benson, A. J., Brodwin, M., Croton, D. J., and Eisenhardt, P. R. (2007). The Evolving Luminosity Function of Red Galaxies. , 654:858–877.

Bruzual, G. and Charlot, S. (2003). Stellar population synthesis at the resolution of 2003. , 344:1000–1028.

Calzetti, D. (1997). UV opacity in nearby galaxies and application to distant galaxies. In Waller, W. H., editor, *American Institute of Physics Conference Series*, volume 408 of *American Institute of Physics Conference Series*, pages 403–412.

Calzetti, D. (2001). The Dust Opacity of Star-forming Galaxies. , 113:1449–1485.

Calzetti, D., Armus, L., Bohlin, R. C., Kinney, A. L., Koornneef, J., and Storchi-Bergmann, T. (2000). The Dust Content and Opacity of Actively Star-forming Galaxies. , 533:682–695.

Canizares, C. R., Fabbiano, G., and Trinchieri, G. (1987). Properties of the X-ray emitting gas in early-type galaxies. , 312:503–513.

Capetti, A. and Baldi, R. D. (2011). Emission lines in early-type galaxies: active nuclei or stars? , 529:A126.

Cardelli, J. A., Clayton, G. C., and Mathis, J. S. (1989). The relationship between infrared, optical, and ultraviolet extinction. , 345:245–256.

Chabrier, G. (2003). Galactic Stellar and Substellar Initial Mass Function. , 115:763–795.

Charlot, S. and Fall, S. M. (2000). A Simple Model for the Absorption of Starlight by Dust in Galaxies. , 539:718–731.

Chilingarian, I. V. and Zolotukhin, I. Y. (2012). A universal ultraviolet-optical colour-colour-magnitude relation of galaxies. , 419:1727–1739.

Cid Fernandes, R., Mateus, A., Sodré, L., Stasińska, G., and Gomes, J. M. (2005). Semi-empirical analysis of Sloan Digital Sky Survey galaxies - I. Spectral synthesis method. , 358:363–378.

Clauset, A., Shalizi, C. R., and Newman, M. E. J. (2009). Power-Law Distributions in Empirical Data. *SIAM Review*, 51:661–703.

Conroy, C. (2013). Modeling the Panchromatic Spectral Energy Distributions of Galaxies. , 51:393–455.

Corbelli, E., Bianchi, S., Cortese, L., Giovanardi, C., Magrini, L., Pappalardo, C., Boselli, A., Bendo, G. J., Davies, J., Grossi, M., Madden, S. C., Smith, M. W. L., Vlahakis, C., Auld, R., Baes, M., De Looze, I., Fritz, J., Pohlen, M., and Verstappen, J. (2012). The Herschel Virgo Cluster Survey. X. The relationship between cold dust and molecular gas content in Virgo spirals. , 542:A32.

da Cunha, E., Charlot, S., and Elbaz, D. (2008). A simple model to interpret the ultraviolet, optical and infrared emission from galaxies. , 388:1595–1617.

da Cunha, E., Eminian, C., Charlot, S., and Blaizot, J. (2010). New insight into the relation between star formation activity and dust content in galaxies. , 403:1894–1908.

Deshmukh, S. P., Tate, B. T., Vagshette, N. D., Pandey, S. K., and Patil, M. K. (2013). A multiwavelength view of the ISM in the merger remnant galaxy Fornax A. *Research in Astronomy and Astrophysics*, 13:885–898.

Deshmukh, S. P., Vagshette, N. D., and Patil, M. K. (2022). Stellar and Dust Properties in a Sample of Blue Early Type Galaxies. *Serbian Astronomical Journal*, 205:23–32.

Djorgovski, S. and Davis, M. (1987). Fundamental properties of elliptical galaxies. , 313:59–68.

Dressel, L. L. (1988). Powerful warm infrared sources in early-type galaxies. , 329:L69–L73.

Faber, S. M., Willmer, C. N. A., Wolf, C., Koo, D. C., Weiner, B. J., Newman, J. A., Im, M., Coil, A. L., Conroy, C., Cooper, M. C., Davis, M., Finkbeiner, D. P., Gerke, B. F., Gebhardt, K., Groth, E. J., Guhathakurta, P., Harker, J., Kaiser, N., Kassin, S., Kleinheinrich, M., Konidaris, N. P., Kron, R. G., Lin, L., Luppino, G., Madgwick, D. S., Meisenheimer, K., Noeske, K. G., Phillips, A. C., Sarajedini, V. L., Schiavon, R. P., Simard, L., Szalay, A. S., Vogt, N. P., and Yan, R. (2007). Galaxy Luminosity Functions to z˜1 from DEEP2 and COMBO-17: Implications for Red Galaxy Formation. , 665:265–294.

Gaibler, V., Khochfar, S., Krause, M., and Silk, J. (2012). Jet-induced star formation in gas-rich galaxies. , 425:438–449.

Ge, C. and Gu, Q.-S. (2012). Peculiar early-type galaxies with central star formation. *Research in Astronomy and Astrophysics*, 12:485–499.

George, K. (2017). Structural analysis of star-forming blue early-type galaxies. Merger-driven star formation in elliptical galaxies. , 598:A45.

George, K. and Zingade, K. (2015). Revealing the nature of star forming blue early-type galaxies at low redshift. , 583:A103.

Gomes, J. M. and Papaderos, P. (2016). RemoveYoung: A tool for the removal of the young stellar component in galaxies within an adjustable age cutoff. , 594:A49.

Goudfrooij, P., Hansen, L., Jorgensen, H. E., and Norgaard-Nielsen, H. U. (1994). Interstellar matter in Shapley-Ames elliptical galaxies. II. The distribution of dust and ionized gas. , 105.

Guo, R., Hao, C.-N., Xia, X. Y., Mao, S., and Shi, Y. (2016). The Role of Major Gas-rich Mergers on the Evolution of Galaxies from the Blue Cloud to the Red Sequence. , 826:30.

Hopkins, A. M., Miller, C. J., Nichol, R. C., Connolly, A. J., Bernardi, M., Gómez, P. L., Goto, T., Tremonti, C. A., Brinkmann, J., Ivezić, Ž., and Lamb, D. Q. (2003). Star Formation Rate Indicators in the Sloan Digital Sky Survey. , 599:971–991.

Huang, S. and Gu, Q.-S. (2009). Recent star-forming activity in local elliptical galaxies. , 398:1651–1667.

Jarrett, T. H., Masci, F., Tsai, C. W., Petty, S., Cluver, M. E., Assef, R. J., Benford, D., Blain, A., Bridge, C., Donoso, E., Eisenhardt, P., Koribalski, B., Lake, S., Neill, J. D., Seibert, M., Sheth, K., Stanford, S., and Wright, E. (2013). Extending the Nearby Galaxy Heritage with WISE: First Results from the WISE Enhanced Resolution Galaxy Atlas. , 145:6.

Kannappan, S. J., Guie, J. M., and Baker, A. J. (2009). E/S0 Galaxies on the Blue Color-Stellar Mass Sequence at z = 0: Fading Mergers or Future Spirals? , 138:579–597.

Kauffmann, G., Heckman, T. M., White, S. D. M., Charlot, S., Tremonti, C., Peng, E. W., Seibert, M., Brinkmann, J., Nichol, R. C., SubbaRao, M., and York, D. (2003). The dependence of star formation history and internal structure on stellar mass for 10^5 low-redshift galaxies. , 341:54–69.

Kaviraj, S., Peirani, S., Khochfar, S., Silk, J., and Kay, S. (2009). The role of minor mergers in the recent star formation history of early-type galaxies. , 394:1713–1720.

Kennicutt, Jr., R. C. (1998). Star Formation in Galaxies Along the Hubble Sequence. , 36:189–232.

Kewley, L. J., Dopita, M. A., Sutherland, R. S., Heisler, C. A., and Trevena, J. (2001). Theoretical Modeling of Starburst Galaxies. , 556:121–140.

Kim, D.-W. and Fabbiano, G. (2010). X-ray Properties of Young Early-type Galaxies. I. X-ray Luminosity Function of Low-mass X-ray Binaries. , 721:1523–1530.

Kokusho, T., Kaneda, H., Bureau, M., Suzuki, T., Murata, K., Kondo, A., and Yamagishi, M. (2017). A star formation study of the ATLAS3D early-type galaxies with the AKARI all-sky survey. *ArXiv e-prints*.

Kong, X., Cheng, F. Z., Weiss, A., and Charlot, S. (2002). Spectroscopic study of blue compact galaxies. II. Spectral analysis and correlations. , 396:503–512.

Kroupa, P. (2001). On the variation of the initial mass function. , 322:231–246.

Kulkarni, S., Sahu, D. K., Chaware, L., Chakradhari, N. K., and Pandey, S. K. (2014). Study of dust and ionized gas in early-type galaxies. , 30:51–63.

Marino, A., Bianchi, L., Rampazzo, R., Thilker, D., Annibali, F., Bressan, A., and Buson, L. M. (2011). Signatures of recent star formation in ring S0 galaxies. , 335:243–248.

McDonald, M., McNamara, B. R., van Weeren, R. J., Applegate, D. E., Bayliss, M., Bautz, M. W., Benson, B. A., Carlstrom, J. E., Bleem, L. E., Chatzikos, M., Edge, A. C., Fabian, A. C., Garmire, G. P., Hlavacek-Larrondo, J., Jones-Forman, C., Mantz, A. B., Miller, E. D., Stalder, B., Veilleux, S., and ZuHone, J. A. (2015). Deep Chandra, HST-COS, and Megacam Observations of the Phoenix Cluster: Extreme Star Formation and AGN Feedback on Hundred Kiloparsec Scales. , 811:111.

Morrissey, P., Conrow, T., Barlow, T. A., Small, T., Seibert, M., Wyder, T. K., Budavári, T., Arnouts, S., Friedman, P. G., Forster, K., Martin, D. C., Neff, S. G., Schiminovich, D., Bianchi, L., Donas, J., Heckman, T. M., Lee, Y.-W., Madore, B. F., Milliard, B., Rich, R. M., Szalay, A. S., Welsh, B. Y., and Yi, S. K. (2007). The Calibration and Data Products of GALEX. , 173:682–697.

Oke, J. B. and Gunn, J. E. (1983). Secondary standard stars for absolute spectrophotometry. , 266:713–717.

Osterbrock, D. E. and Ferland, G. J. (2006). *Astrophysics of gaseous nebulae and active galactic nuclei*.

Pandge, M. B., Vagshette, N. D., David, L. P., and Patil, M. K. (2012). Systematic study of X-ray cavities in the brightest galaxy in the Draco constellation NGC 6338. , 421:808–817.

Panuzzo, P., Rampazzo, R., Bressan, A., Vega, O., Annibali, F., Buson, L. M., Clemens, M. S., and Zeilinger, W. W. (2011). Nearby early-type galaxies with ionized gas. VI. The Spitzer-IRS view. Basic data set analysis and empirical spectral classification. , 528:A10.

Patil, M. K., Pandey, S. K., Sahu, D. K., and Kembhavi, A. (2007). Properties of dust in early-type galaxies. , 461:103–113.

Phillips, M. M., Jenkins, C. R., Dopita, M. A., Sadler, E. M., and Binette, L. (1986). Erratum - Ionized Gas in Elliptical and so Galaxies - Part One - a Survey for Hα and NII Emission. , 92:503.

Pinto, C., Fabian, A. C., Werner, N., Kosec, P., Ahoranta, J., de Plaa, J., Kaastra, J. S., Sanders, J. S., Zhang, Y.-Y., and Finoguenov, A. (2014). Discovery of O VII line emitting gas in elliptical galaxies. , 572:L8.

Renzini, A. and Peng, Y.-j. (2015). An Objective Definition for the Main Sequence of Star-forming Galaxies. , 801:L29.

Salim, S. (2014). Green Valley Galaxies. *Serbian Astronomical Journal*, 189:1–14.

Salim, S., Lee, J. C., Davé, R., and Dickinson, M. (2015). On the Mass-Metallicity-Star Formation Rate Relation for Galaxies at z
2. , 808:25.

Salim, S., Rich, R. M., Charlot, S., Brinchmann, J., Johnson, B. D., Schiminovich, D., Seibert, M., Mallery, R., Heckman, T. M., Forster, K., Friedman, P. G., Martin, D. C., Morrissey, P., Neff, S. G., Small, T., Wyder, T. K., Bianchi, L., Donas, J., Lee, Y.-W., Madore, B. F., Milliard, B., Szalay, A. S., Welsh, B. Y., and Yi, S. K. (2007). UV Star Formation Rates in the Local Universe. , 173:267–292.

Schawinski, K., Urry, C. M., Simmons, B. D., Fortson, L., Kaviraj, S., Keel, W. C., Lintott, C. J., Masters, K. L., Nichol, R. C., Sarzi, M., Skibba, R., Treister, E., Willett, K. W., Wong, O. I., and Yi, S. K. (2014). The green valley is a red herring: Galaxy Zoo reveals two evolutionary pathways towards quenching of star formation in early- and late-type galaxies. , 440:889–907.

Schawinski, K., Urry, C. M., Virani, S., Coppi, P., Bamford, S. P., Treister, E., Lintott, C. J., Sarzi, M., Keel, W. C., Kaviraj, S., Cardamone, C. N., Masters, K. L., Ross, N. P., Andreescu, D., Murray, P., Nichol, R. C., Raddick, M. J., Slosar, A., Szalay, A. S., Thomas, D., and Vandenberg, J. (2010). Galaxy Zoo: The Fundamentally Different Co-Evolution of Supermassive Black Holes and Their Early- and Late-Type Host Galaxies. , 711:284–302.

Schiminovich, D., Wyder, T. K., Martin, D. C., Johnson, B. D., Salim, S., Seibert, M., Treyer, M. A., Budavári, T., Hoopes, C., Zamojski, M., Barlow, T. A., Forster, K. G., Friedman, P. G., Morrissey, P., Neff, S. G., Small, T. A., Bianchi, L., Donas, J., Heckman, T. M., Lee, Y.-W., Madore, B. F., Milliard, B., Rich, R. M., Szalay, A. S., Welsh, B. Y., and Yi, S. (2007). The UV-Optical Color Magnitude Diagram. II. Physical Properties and Morphological Evolution On and Off of a Star-forming Sequence. , 173:315–341.

Schlegel, D. J., Finkbeiner, D. P., and Davis, M. (1998). Maps of Dust Infrared Emission for Use in Estimation of Reddening and Cosmic Microwave Background Radiation Foregrounds. , 500:525–553.

Skrutskie, M. F., Cutri, R. M., Stiening, R., Weinberg, M. D., Schneider, S., Carpenter, J. M., Beichman, C., Capps, R., Chester, T., Elias, J., Huchra, J., Liebert, J., Lonsdale, C., Monet, D. G., Price, S., Seitzer, P., Jarrett, T., Kirkpatrick, J. D., Gizis, J. E., Howard, E., Evans, T., Fowler, J., Fullmer, L., Hurt, R., Light, R., Kopan, E. L., Marsh, K. A., McCallon, H. L., Tam, R., Van Dyk, S., and Wheelock, S. (2006). The Two Micron All Sky Survey (2MASS). , 131:1163–1183.

Smith, D. J. B., Dunne, L., da Cunha, E., Rowlands, K., Maddox, S. J., Gomez, H. L., Bonfield, D. G., Charlot, S., Driver, S. P., Popescu, C. C., Tuffs, R. J., Dunlop, J. S., Jarvis, M. J., Seymour, N., Symeonidis, M., Baes, M., Bourne, N., Clements, D. L., Cooray, A., De Zotti, G., Dye, S., Eales, S., Scott, D., Verma, A., van der Werf, P., Andrae, E., Auld, R., Buttiglione,

S., Cava, A., Dariush, A., Fritz, J., Hopwood, R., Ibar, E., Ivison, R. J., Kelvin, L., Madore, B. F., Pohlen, M., Rigby, E. E., Robotham, A., Seibert, M., and Temi, P. (2012). Herschel-ATLAS: multi-wavelength SEDs and physical properties of 250 μm selected galaxies at z 0.5. , 427:703–727.

Smith, D. J. B. and Hayward, C. C. (2015). Deriving star formation histories from photometry using energy balance spectral energy distribution modelling. , 453:1597–1607.

Sonkamble, S. S., Vagshette, N. D., Pawar, P. K., and Patil, M. K. (2015). X-ray cavities and temperature jumps in the environment of the strong cool core cluster Abell 2390. , 359:21.

Strateva, I., Ivezić, Ž., Knapp, G. R., Narayanan, V. K., Strauss, M. A., Gunn, J. E., Lupton, R. H., Schlegel, D., Bahcall, N. A., Brinkmann, J., Brunner, R. J., Budavári, T., Csabai, I., Castander, F. J., Doi, M., Fukugita, M., Győry, Z., Hamabe, M., Hennessy, G., Ichikawa, T., Kunszt, P. Z., Lamb, D. Q., McKay, T. A., Okamura, S., Racusin, J., Sekiguchi, M., Schneider, D. P., Shimasaku, K., and York, D. (2001). Color Separation of Galaxy Types in the Sloan Digital Sky Survey Imaging Data. , 122:1861–1874.

Summers, L. K., Stevens, I. R., Strickland, D. K., and Heckman, T. M. (2004). Chandra and XMM-Newton observations of NGC 5253: analysis of the X-ray emission from a dwarf starburst galaxy. , 351:1–17.

Taylor, E. N., Hopkins, A. M., Baldry, I. K., Brown, M. J. I., Driver, S. P., Kelvin, L. S., Hill, D. T., Robotham, A. S. G., Bland-Hawthorn, J., Jones, D. H., Sharp, R. G., Thomas, D., Liske, J., Loveday, J., Norberg, P., Peacock, J. A., Bamford, S. P., Brough, S., Colless, M., Cameron, E., Conselice, C. J., Croom, S. M., Frenk, C. S., Gunawardhana, M., Kuijken, K., Nichol, R. C., Parkinson, H. R., Phillipps, S., Pimbblet, K. A., Popescu, C. C., Prescott, M., Sutherland, W. J., Tuffs, R. J., van Kampen, E., and Wijesinghe, D. (2011). Galaxy And Mass Assembly (GAMA): stellar mass estimates. , 418:1587–1620.

Temi, P., Brighenti, F., and Mathews, W. G. (2009). Spitzer Observations of Passive and Star-Forming Early-Type Galaxies: An Infrared Color-Color Sequence. , 707:890–902.

Tosi, M., Greggio, L., Marconi, G., and Focardi, P. (1991). Star formation in dwarf irregular galaxies - Sextans B. , 102:951–974.

Vaddi, S., O'Dea, C. P., Baum, S. A., Whitmore, S., Ahmed, R., Pierce, K., and Leary, S. (2016). Constraints on Feedback in the Local Universe: The Relation between Star Formation and AGN Activity in Early-type Galaxies. , 818:182.

Vagshette, N. D., Pandge, M. B., Pandey, S. K., and Patil, M. K. (2012). Dust extinction and X-ray emission from the starburst galaxy NGC 1482. , 17:524–532.

Vagshette, N. D., Pandge, M. B., and Patil, M. K. (2013). Spectral properties of XRBs in dusty early-type galaxies. , 21:1–7.

Wei, L. H., Kannappan, S. J., Vogel, S. N., and Baker, A. J. (2010). Gas Mass Fractions and Star Formation in Blue-Sequence E/S0 Galaxies. , 708:841–861.

Wright, E. L., Eisenhardt, P. R. M., Mainzer, A. K., Ressler, M. E., Cutri, R. M., Jarrett, T., Kirkpatrick, J. D., Padgett, D., McMillan, R. S., Skrutskie, M., Stanford, S. A., Cohen, M., Walker, R. G., Mather, J. C., Leisawitz, D., Gautier, III, T. N., McLean, I., Benford, D., Lonsdale, C. J., Blain, A., Mendez, B., Irace, W. R., Duval, V., Liu, F., Royer, D., Heinrichsen, I., Howard, J., Shannon, M., Kendall, M., Walsh, A. L., Larsen, M., Cardon, J. G., Schick, S., Schwalm, M., Abid, M., Fabinsky, B., Naes, L., and Tsai, C.-W. (2010). The Wide-field Infrared Survey Explorer (WISE): Mission Description and Initial On-orbit Performance. , 140:1868–1881.

Wyder, T. K., Martin, D. C., Schiminovich, D., Seibert, M., Budavári, T., Treyer, M. A., Barlow, T. A., Forster, K., Friedman, P. G., Morrissey, P., Neff, S. G., Small, T., Bianchi, L., Donas, J., Heckman, T. M., Lee, Y.-W., Madore, B. F., Milliard, B., Rich, R. M., Szalay, A. S., Welsh, B. Y., and Yi, S. K. (2007). The UV-Optical Galaxy Color-Magnitude Diagram. I. Basic Properties. , 173:293–314.

Yi, S. K., Yoon, S.-J., Kaviraj, S., Deharveng, J.-M., Rich, R. M., Salim, S., Boselli, A., Lee, Y.-W., Ree, C. H., Sohn, Y.-J., Rey, S.-C., Lee, J.-W., Rhee, J., Bianchi, L., Byun, Y.-I., Donas, J., Friedman, P. G., Heckman, T. M., Jelinsky, P., Madore, B. F., Malina, R., Martin, D. C., Milliard, B., Morrissey, P., Neff, S., Schiminovich, D., Siegmund, O., Small, T., Szalay, A. S., Jee, M. J., Kim, S.-W., Barlow, T., Forster, K., Welsh, B., and Wyder, T. K. (2005). Galaxy Evolution Explorer Ultraviolet Color-Magnitude Relations and Evidence of Recent Star Formation in Early-Type Galaxies. , 619:L111–L114.